

# The effect of the Pliocene regional climate changes temperature pattern on silicate weathering : ~~a potential amplifier of and~~ Pliocene-Pleistocene cooling

Pierre Maffre<sup>1</sup>, John C. H. Chiang<sup>1</sup>, and Nicholas L. Swanson-Hysell<sup>1</sup>

<sup>1</sup>University of California, Berkeley

**Correspondence:** Pierre Maffre (maffre@berkeley.edu)

## Abstract.

The warmer early Pliocene climate featured changes to global sea surface temperature (SST) patterns, namely a reduction to the equator-pole gradient and to the east-west SST gradient in the tropical Pacific, the so-called “permanent El Niño”. Here we investigate the consequences of the SST changes to silicate weathering and thus to atmospheric CO<sub>2</sub> on geological timescales.

5 Different SST patterns than today imply regional modifications of the hydrological cycle that directly affects continental silicate weathering in particular over tropical “hotspots” of weathering such as the Maritime continent, thus leading to a “weatherability pattern effect”. We explore the impact of ~~Pliocene-Pliocene-like~~ SST changes on weathering using climate model and silicate weathering model simulations, and deduce CO<sub>2</sub> and temperature at carbon cycle equilibrium between solid Earth degassing and silicate weathering. In general, we find large regional increases and decreases to weathering fluxes ~~that largely cancel out~~

10 ~~one another. For permanent and the net effect depends on the extent to which they cancel. Permanent~~ El Niño conditions ; ~~weathering decreases outweigh the increases, leading lead~~ to a small amplification of warming relative to the present-day by 0.4 °C. ~~The, suggesting that the~~ demise of permanent El Niño could have had a small amplifying effect on cooling from the early Pliocene into the Pleistocene. For the reduced equator-pole gradient, the weathering increases and decreases largely cancel leading to no detectable difference in global temperature at carbon cycle equilibrium. A robust SST reconstruction of

15 the Pliocene is needed for a quantitative evaluation of the weatherability pattern effect.

## 1 Introduction

Evidence has been accumulating that east-west (zonal) gradients of sea surface temperature (SST) and thermocline depth in the tropical Pacific were reduced during the warm early Pliocene (4.5 – 3 Ma) with respect to modern conditions (e.g., ???). These features, resembling modern El Niño events, have led to the idea of a “permanent El Niño” climatic state during the

20 Pliocene epoch, also named “El Padre” (?). Paleoclimate proxy data also supports that the average equator-pole (meridional) temperature gradient was reduced during the warm early Pliocene (???)

The transition between early Pliocene to modern climate conditions is thought to be linked to global cooling from the Pliocene (5.3 to 2.6 Ma) into the Pleistocene (2.6 to 0.01 Ma), both as a cause or a consequence. This global cooling since the Pliocene has occurred while there is little evidence of significant change in CO<sub>2</sub> outgassing (e.g., ?), suggesting another

25 trigger. ? argued that the onset of a modern tropical Pacific zonal SST gradient (due to the larger cooling of the eastern tropical Pacific) may have permitted the inception of the Laurentide ice sheet, promoting global cooling. In this hypothesis, teleconnection altered the atmospheric circulation over North America thereby enabling accumulation of perennial snow in winter in northern North America. The authors developed the hypothesis that vigorous modern Pacific Walker circulation – ~~which enhanced the zonal SST gradient~~ – was caused by the restriction of the Indonesian seaway as well as the increased  
30 land area of emerged islands in the Maritime Continent, both due to tectonic processes associated with arc-continent collision. The Walker circulation is an east-west atmospheric overturning circulation near the equator, that interacts with an oceanic counterpart, setting up a zonal SST gradient across the ocean basin. On the other hand, ? proposed a feedback loop where shoaling of the thermocline with cooling climate activates the Bjerknes feedback ~~and thus invigorates~~ – the amplification of the cooling of the eastern boundary of a equatorial basin through upwelling of cold water due to easterly winds. This feedback  
35 promotes easterlies thus invigorating the Walker circulation, ~~and~~ further enhancing climate cooling through cloud-albedo and ice-albedo feedback. The zonal tropical Pacific SST gradient has also been shown to be linked to the global meridional temperature gradient (?). Therefore, all the following elements, strengthening zonal and meridional gradients, intensification of El Niño Southern Oscillation (ENSO), onset of a mean climate state closer to La Niña, and global cooling, would be ~~part of a same process~~ connected processes.

40 One element that has been largely overlooked in these considerations about regional climate changes is their effect on silicate weathering and the silicate weathering feedback. The so-called silicate weathering paleothermostat (?) is the hypothesis that long-term climate is controlled by the balance between deep earth degassing of CO<sub>2</sub> and its consumption by continental silicate weathering and associated oceanic carbonate precipitation (the Urey reaction, ?). Weathering reactions are enhanced by warmer climate which introduces a negative feedback: atmospheric CO<sub>2</sub> is stabilized at the level where its consumption balances its  
45 degassing (??). Continental runoff rate is a key factor controlling silicate weathering rate (????). The very existence of the silicate weathering paleothermostat relies to a large extent on the fact that runoff rates, on average, increase with rising CO<sub>2</sub> and associated global warming (?). Hence, processes that affect the distribution of continental runoff, even without direct effects on global temperature, have the potential to change the efficiency of silicate weathering, and therefore, equilibrium atmospheric CO<sub>2</sub> level, and global temperature. This phenomenon is analogous to the so-called “pattern effect” (?) in the  
50 Earth’s temperature climate sensitivity to atmospheric CO<sub>2</sub>. As with climate sensitivity, SST patterns may have significant effects on the efficiency of silicate weathering – hereafter called “weatherability” – because they affect atmospheric convection, precipitation and runoff.

In that regard, reducing meridional or zonal SST gradients (with respect to modern climate) may decrease global weatherability by shifting rainfall away from tropical land masses. In the case of meridional gradient, ? suggested a reduced equatorward  
55 moisture transport by the Hadley circulation with flatter SST gradient. This feature can be summarized by “wet gets dryer, dry gets wetter” (?). In the case of zonal ~~gradient~~ gradients, a weaker Pacific gradient should lead to reduced Pacific Walker circulation, that is responsible of intense precipitation over the Maritime continent in modern climate. Indeed, El Niño events, where the Pacific Walker circulation collapses, leads to a drastic decrease of continental runoff on the Maritime continent, as well as most of South America near the equator (see Fig. ~~??-1~~ 1 showing the El Niño-years climatology of precipitation and

60 runoff). On average, runoff is reduced by  $\sim 3\%$  on land during El Niño-years. The key element here is that some tropical areas that are drier in El Niño years, are known hotspots of silicate weathering – mainly, the Southeast Asian Islands known as the Maritime continent (Figs. ~~?? and ??~~ 1 and 2a). Another contribution to changes in silicate weathering should be expected from the Himalaya and the portion of the Andes north of the equator, that also experience decreases in runoff during El Niño years.

The above text and associated hypothesis can be summarized as: “With weaker meridional and zonal temperature gradients, 65 the decrease of runoff over land, specifically on tropical weathering hotspots, would lead to reduced weatherability and, as a result, higher CO<sub>2</sub> levels contributing to the warmer Pliocene climate.” If we further assume that colder climate favors stronger meridional and zonal gradients, the overall process of cooling would act as a positive feedback loop where increased cooling leads to increased precipitation on key land masses, which would lead to enhanced weatherability and increased cooling. This process has the potential to have amplified climate cooling from the warm early Pliocene into the Pleistocene.

70 In this contribution, we investigate the potential effect of meridional and zonal gradients on global climate through the silicate weathering feedback, without seeking to determine the cause of these regional climate features. We first provide an estimation of the silicate weathering anomaly using the climate fields from ERA5 reanalysis 1979–2020 (??), with the assumption that the average climate of El Niño events ~~is a good representation of~~ can be used as a proxy for Pliocene permanent El Niño. This method enables a qualitative assessment of whether the effect of a permanent El Niño state on global chemical weathering 75 would generate a warmer or colder global climate (because of a decrease or an increase of chemical weathering, respectively). However, one cannot quantitatively estimate this warming or cooling because the climate reanalysis only exist at current CO<sub>2</sub> ~~levels, yet, if silicate weathering is disturbed,~~ level. Yet, any disturbance in the efficiency of silicate weathering – that is, increase or decrease of silicate weathering flux at current CO<sub>2</sub> ~~will adjust to restore the carbon cycle level – will change~~ CO<sub>2</sub> until the balance between CO<sub>2</sub> degassing and its consumption by silicate weathering is restored. On the million-years timescale 80 of ~~Pliocene to the~~ Pliocene to the modern, it is this equilibrium CO<sub>2</sub> level that matters for climate evolution. Furthermore, it is possible that the average of El Niño years is not a perfect analog of a permanent El Niño, because of the transient nature of those events, and the fact that they are not bound to radiative balance, as is a long-term equilibrium climate state.

For these two reasons, we designed numerical climate experiments aimed at ~~reproducing~~ exploring Pliocene climate features with a climate model, focusing on the meridional and the zonal tropical SST gradient. Doing so, we provide ~~a~~ an initial 85 quantitative estimation of the role of a “weatherability pattern effect” on climate evolution since the warm early Pliocene, through the silicate weathering feedback.

## 2 Methods

### 2.1 Silicate weathering model

We use the silicate weathering model published in ?. This model represents the steady-state vertical profile of primary silicate 90 minerals abundance in a regolith – the interface between unweathered bedrock and land surface. Minerals are progressively weathered until they are removed from the regolith through physical erosion of the surface. Hence, weathering profiles show a continuous depletion of primary minerals from bedrock to the surface. The vertically-integrated weathering rate depends

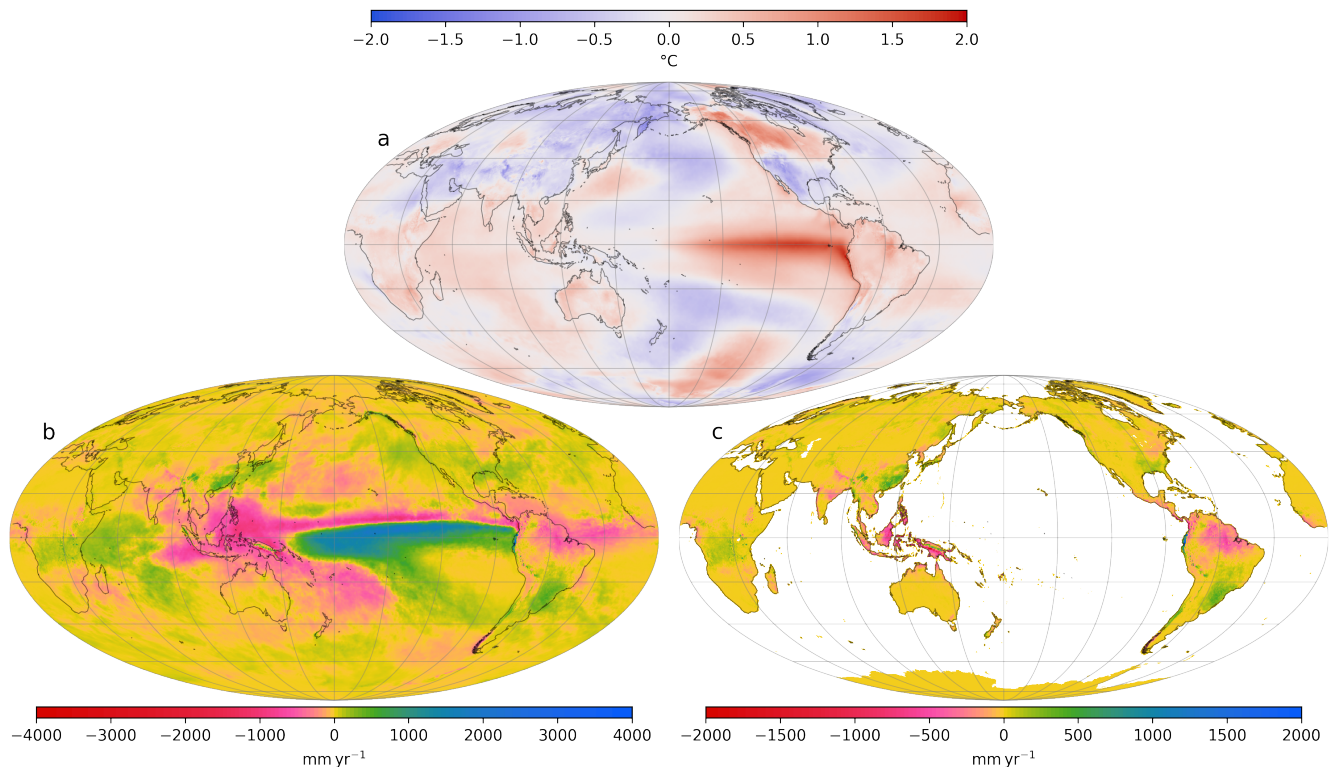


**Figure 1.** Differences in climatology associated with El Niño years. (a): anomaly of temperature, average of selected El Niño years (minus average of years selected neither as El Niño nor as La Niña. Each “year” considered here is from May to the following April) minus the full climatology average, data. Data is from ERA5 reanalysis (see, See Methods, section 2.2, and Appendix A for details). (a): 2 m temperature, (b): total precipitation, and (c): continental runoff. On each panel, non-significant differences are hatched (p-value of Welch’s t-test  $> 0.1$ , see Appendix C). The maps are Mollweide projections with graticules plotted every  $30^\circ$  of longitude and every  $20^\circ$  of latitude (both starting from  $0^\circ$ ). (b): same El Niño anomaly as in (a) for total precipitation. (c): same El Niño anomaly as (a) for continental runoff. Note that it is significantly drier over the South-East Asian Islands in El Niño years with more precipitation falling over the tropical Pacific ocean rather than over land.

on the rate of physical erosion (which leads to upward advection of primary minerals), the efficiency of weathering chemical reactions (that depend on runoff and temperature), and the residence time of minerals in the regolith (that is also controlled by the physical erosion rate). The derivation of this model was carried out by ? and ?, who parameterized the climatic control of weathering reactions (through temperature and runoff). The erosion rate is computed as a power-law of topographic slope and runoff rate (??).

The value of interest computed by the weathering model is the amount of dissolved Ca and Mg released by weathering of silicates-silicate minerals (integrated over the regolith profile). This flux corresponds to long-term  $\text{CO}_2$  consumption in the geological carbon cycle through the eventual precipitation of marine carbonates. The weathering model is applied on

every point of the continental mesh grid, at the resolution of the climate fields used (see following sections). On each point, computation of the estimated weathering rate is done for 5 lithological classes of silicates (as in ?) that are simplified from the global lithological map of ?. The slope field was derived from the elevation dataset of the Shuttle Radar Topography Mission (?) at 30" resolution. Both the lithological classes and the slope were interpolated on the desired mesh grids.

105 The model parameters are taken from ? who provided an ensemble of 573 “best-fit” unique parameter combinations resulting from a comparison of model results to modern chemical weathering fluxes across watersheds. ~~Similarly to As in ?~~, the weathering model is run with all those unique parameter combinations. We present, for each model run, the ensemble of results (e.g., the ensemble of the global weathering flux). This approach allows us to quantify the uncertainties arising from the weathering parameters.

110 The silicate weathering model does not explicitly represent the role of vegetation as a weathering agent. Yet, because it is calibrated with data from natural systems, the parameters incorporate a part of the vegetation effects embedded in the data. For instance, the values of parameters determining the sensitivity to the runoff ( $k_d$  and  $k_w$ ) are influenced by the correlation between water availability and the presence of vegetation.

## 2.2 Climate reanalysis and selection of El Niño and La Niña years

115 The reanalysis climate fields used in this study are from ERA5-land 1981–2019 (?) for continental runoff, and ERA5 1979–2020 (?) for 2 m temperature and SST. The monthly averaged fields at the native resolution ( $0.1^\circ$  for ERA5-land and  $0.25^\circ$  for ERA5) were interpolated on a longitude-latitude grid of  $0.5^\circ$  resolution.

To determine the climatology associated with El Niño and La Niña years, we ~~generate~~ generated an interannual index of ENSO, and then ~~use~~ used it to create ~~composite selections of El Niño and years~~, La Niña years. ~~The generation of the index proceeded as follows: we used the detrended monthly SST average on Niño 3 region, that is,  $-(?)$ . We detrended the time-series by performing a linear regression with respect to time, and subtracted the “time” term from the original time-series. We grouped the monthly time-series in “year” vectors of 12 elements, corresponding to the 12 months, from May to April of the next calendar year. We subtracted to each year vector the average of all years, to center the vectorial time-series. We then performed a principal component analysis. We identified the first eigenvector (or EOF, for empirical orthogonal function) as~~  
120 ~~the signature of~~ and neither El Niño events. We projected the detrended, centered, vectorial time-series on this first EOF (scalar product of the two 12 elements vectors, for each year). We normalized the scalar time-series obtained in this way by dividing it by its standard deviation (across the years). This normalized time-series can be interpreted as a time-series of the El Niño index for each year. We selected the El Niño years as the years having an index  $> 0.9$ , and  $< -0.9$  for the La ~~nor~~ La Niña years.

~~Based on the described procedure~~ The details of the calculation of this ENSO index can be found in Appendix A. Based on  
130 this index, we selected the years 1982, 1987, 1991, 1997, 2009 and 2015 as El Niño years, and the years 1984, 1988, 1999, 2007 and 2010 La Niña years (in each case, from May to April of the next calendar year).

## 2.3 Climate model

~~Summary of all the climate simulations presented in this study~~

~~Name boundary conditions\* ocean model level (-) integration time~~  
135 ~~COA-ctrl-pre-industrial full~~  
~~COA-Plio-modified cloud albedo full~~  
~~fSST-ctrl-pre-industrial fixed SST~~  
~~fSST-Plio-full SST from “COA-Plio” fixed SST ; ; ;~~  
~~fSST-Plio-10SN-SST from “COA-Plio” fixed SST ; ; ;~~  
140 ~~control pre-industrial slab ; ; ; ;~~  
~~full Pliocene SST Q flux derived from “fSST-Plio-full” slab ; ; ; ;~~  
~~Pliocene SST Q flux derived from “fSST-Plio-10SN” slab ; ; ; ;~~

For the climate numerical experiments, we used the Community Earth System Model (CESM) version 1.2.2.1. The experiments were conducted using the components CAM4 for the atmospheric dynamics, CLM4.0 land model, CLM4.0 CN  
145 river-runoff component, CICE prognostic sea ice, and for the oceanic component, either fixed SSTk DOCN in slab ocean mode, or full ocean model (Parallel Ocean Program version 2). The slab ocean approximates a well-mixed ocean mixed layer with a fixed depth set to the annual mean; an ocean heat transport convergence (i.e., the “Q flux”) from a CESM1 pre-industrial fully coupled run is prescribed at each ocean gridpoint to achieve a simulated sea surface temperature close to the pre-industrial. The grids used are a regular  $0.9^\circ \times 1.25^\circ$  (latitude  $\times$  longitude) for atmosphere and land modules, a regular  $0.5^\circ$  for runoff  
150 routing, and a  $\sim 1^\circ$  “displaced” grid, with Greenland pole, (0.9x1.25\_gxlv6) for the ocean models (both slab and full) and sea ice modules.

All experiments were conducted with permanent 1850 (pre-industrial) boundary conditions, with the exception of the few modifications discussed later in the article, that are atmospheric CO<sub>2</sub> concentration, slab ocean Q flux, and clouds albedo. Experiments were run 40 years for the fixed SST cases, 50 years for the slab ocean cases, and 230 years (170 years for the  
155 control) for the coupled ocean-atmosphere cases. All experiments were initiated with a “cold start” (internally-generated initial condition, corresponding to a pre-industrial climate). In all cases, the last 30 years of the model runs were used to compute the climatology average. ~~Table B1 summarized~~ [See Table B1 and Appendix B for more information about](#) the specific features of ~~all~~ the climate simulations conducted here.

## 2.4 Geographic division of silicate weathering

160 ~~Map of the geographic division used to summarize results in this study (colored semi-transparent shades) superimposed on land topography. The map is a Mollweide projection (equal area) with parallels drawn every and meridians every , both starting from .~~

To quantify the contributions of the different regions of Earth to the changes of silicate weathering flux due to perturbations of climate fields, we used the geographic division shown in Fig. ~~??~~2a. This division is meant to isolate known weathering  
165 hotspots (e.g. Maritime Continent and East African rift), major mountain ranges, and, for the remaining regions, tropics versus subtropics. The boundaries of these regions are somewhat arbitrary, especially for the mountain ranges, and their naming should be considered as a simplification of the broader regions. For instance, “Himalaya” refer to the merging of the Himalayan range,

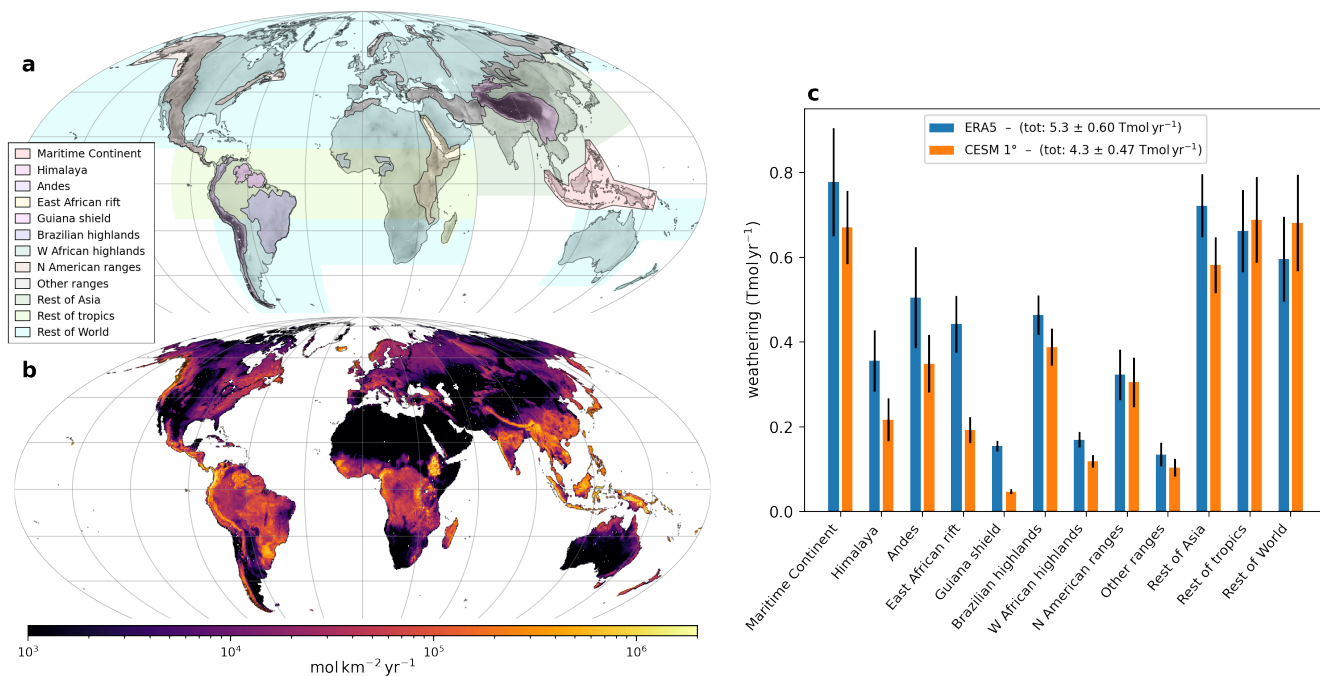


**Figure 2.** (a): Map of the geographic division used to summarize results in this study (colored semi-transparent shades) superimposed on land topography. (b): Average chemical weathering rates (Ca and Mg from silicate minerals) over the parameter combinations (i.e., the weathering model is run for each of the 573 selected parameter combination, and the 573 weathering fields are then averaged). Weathering is computed using climate fields from ERA5 reanalysis (climatology average 1981–2019) at  $0.5^\circ$  of resolution. (c): Bar plot of chemical weathering fluxes integrated over the geographic regions (panel a), using ERA5 climate fields – as for panel (b) (blue bars); or using climate fields from CESM1.2 climate model pre-industrial control simulation, with slab ocean model, performed in this study (average of last 30 years simulations; orange bars). The main colored bars denote the average weathering flux of the 573 parameterizations, whereas the black error bars denote the standard deviation over those parameterizations. The total (summed) weathering flux is indicated on the legend box giving both the average and associated standard-deviation resulting from the different weathering model parameterizations. The maps projection and graticules (panels a and b) are similar to Fig. 1

its extension over the Longmen Shan and in South-East Asia, the Tibetan plateau and the Tian Shan. Despite the subjectivity of those boundaries, these divisions give a sense of the different response of individual regions that are useful for summarizing results.

### 3 Results

#### 3.1 Weathering rates using ERA5 reanalysis

##### 3.1.1 Control simulation

175 ~~Average chemical weathering rates (and from silicate minerals) over the parameter combinations (i.e., the weathering model is run for each of the 573 selected parameter combination, and the 573 weathering fields are then averaged). Weathering is computed using climate fields from ERA5 reanalysis (climatology average 1981–2019) at of resolution. Map projection and graticules are the same as in Fig. ??.~~

We first run the weathering model using ERA5 reanalysis of climate fields (1981–2019 climatology average), as a control simulation. The resulting weathering rates (averaged over the selected parameterizations) are presented in on a map in Fig. 2b. The total CO<sub>2</sub> consumption by weathering is 5.3 Tmol yr<sup>-1</sup>. This control weathering field is very similar to the one published in (? , Fig. S5 of their contribution), who used the same model, parameter combinations and slope fields, but different climate fields ([CRU TS v.4.03 for the temperature, ?](#), and [UNH/GRDC Composite Runoff Fields V1.0, ?](#)).

185 ~~Bar plot of chemical weathering fluxes integrated over the geographic regions shown in Fig. ??, using climate fields from ERA5 reanalysis (1981–2019 average, of resolution, blue bars), or CESM1.2 climate model pre-industrial control simulation (with slab ocean model) performed in this study (average of last 30 years simulations, of resolution, orange bars). The main colored bars denote the average weathering flux of the 573 parameterizations, whereas the black error bars denote the standard deviation over those parameterizations. The total (summed) weathering flux is indicated on the legend box giving both the average and associated standard deviation resulting from the different weathering model parameterizations.~~

The contribution of the different regions of Earth to this control weathering flux is shown in Fig. 2c (blue bars). The weathering flux from the Maritime Continent is about 11% of the total flux, which is consistent with previous estimates (e.g., ?). The main mountain belts (broader Himalaya, Andes and North and central American ranges, including the rocky mountains) together contribute to ~ 22% of the total. Another significant weathering contributor is the East African Rift (~ 8% of the total), owing to relatively high runoff rates, the substantial amount mafic silicate rocks exposed, and ~~to~~ the relatively steep topography ~~fostering that fosters physical~~ erosion – and hence, ~~chemical weathering~~ [elevated chemical weathering fluxes](#). Taiwan and New Zealand, that are known hotspots of [physical](#) erosion rates, do not contribute significantly to the total [chemical](#) weathering flux because of the limited areal extent of their orogens.

### 3.1.2 El Niño and La Niña years climatologies

200 ~~Bar plot of the anomaly of weathering flux integrated over the geographic regions shown in Fig. ?? with respect to ERA5 control weathering (blue bars in Fig. ??) for El Niño or La Niña years climatology, using ERA5 reanalysis. Average (main colored bars) and standard deviation (error bars) refers to the parameterizations, as in Fig. ??.~~ The change in weathering rate is most dramatic over the Maritime Continent due to increased precipitation over land during La Niña years compared to being over the Pacific Ocean during El Niño years

We then recompute the weathering rates with the same dataset, but keeping only the years of the climate time-series identified as “El Niño” or “La Niña” (average of May to April, see Methods, section 2.2). The anomaly of Earth-integrated weathering flux is  $-90 \pm 15.4$  Gmol yr<sup>-1</sup> for El Niño years and  $+138 \pm 30.1$  Gmol yr<sup>-1</sup> for La Niña (“±” denoting the standard deviation of the weathering anomaly over the selected parameterizations). [These calculations are assuming that these climatologies are imposed over a long-timescale such that the chemical weathering profiles adjust to result in these fluxes. Assuming that](#) CO<sub>2</sub>



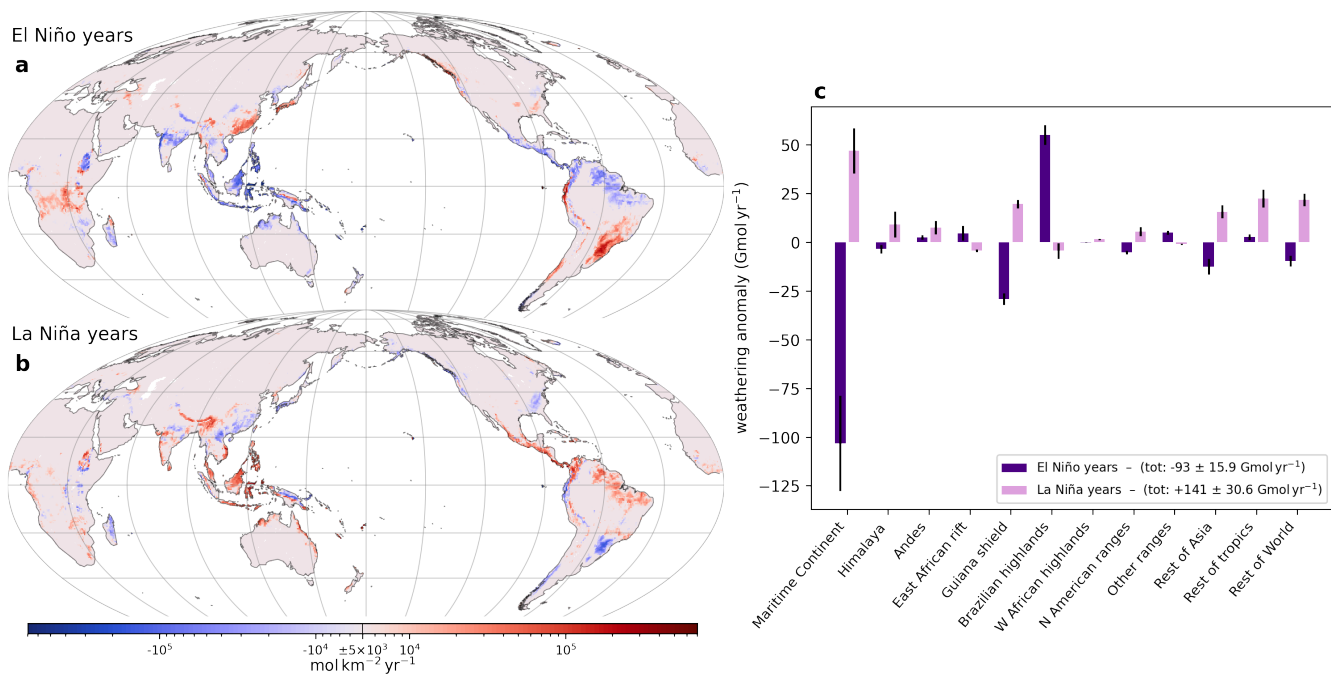


**Figure 3.** (a) and (b): Anomaly of modeled weathering rate with respect to control weathering (i.e., the field displayed shown in Fig. ??2b) for a: El Niño years climatology (a) and b: La Niña years climatology (b). The weathering rate is averaged over the parameter combinations (as in Fig. ??2b). The colorbar scale is a “symmetric logarithm”, and any value lower than  $5 \cdot 10^3 \text{ mol km}^{-2} \text{ yr}^{-1}$  (in absolute value) is approximated as 0. Map projection and graticules are as in to Figs Fig. ??-1. (c): Bar plot of the anomaly of weathering flux integrated over the geographic regions shown in Fig. 2a with respect to ERA5 control weathering (blue bars in Fig. 2c) for El Niño or La Niña years climatology. Average (main colored bars) and ??standard deviation (error bars) refer to the parameterizations, as in Fig. 2c. There are many regional changes of note as discussed in the text. For example, there is enhanced weathering over the Maritime continent during La Niña years relative to El Niño years (see summary - The change in Fig weathering rate is most dramatic over the Maritime Continent due to increased precipitation over land during La Niña years compared to being over the Pacific Ocean during El Niño years.??)

degassing is constant, these weathering anomalies would in reality be compensated by global warming or cooling, so that the net silicate weathering flux anomaly is zero. If we extrapolate from the silicate weathering feedback computed with CESM climate

210 simulations (see also Fig. ??), these weathering anomalies would correspond to, indicating a global weathering flux increase of  $\sim 0.4 \text{ Tmol yr}^{-1}$  per  $^{\circ}\text{C}$  of global warming by  $\text{CO}_2$  (Fig. 8b, solid black curve), the weathering anomalies should then be compensated by global mean temperature anomalies of for the  $+0.23 \text{ }^{\circ}\text{C}$  for long-term El Niño conditions and  $-0.35 \text{ }^{\circ}\text{C}$  for long-term La Niña conditions. These relatively small values of weathering anomaly (1.7% and 2.6% of the total control flux, respectively) are the consequences of local increase and decrease of weathering rates that compensate each other (Fig. 3).  
 215 Nevertheless, the differences from 0 are robust among all the selected parameterizations (the absolute anomaly of weathering flux is  $\sim 4$  times larger than the standard deviation due to the parameter uncertainties), and approximately symmetrical between

El Niño and La Niña conditions. These results support our hypothesis of climate cooling caused by the progressive onset of “La Niña-like” mean climatic conditions, though the magnitude of this cooling may not have been substantial.

Local weathering anomalies are largely driven by changes in runoff rates. Many regions display dipolar patterns under El Niño conditions (Fig. 3a). For example, weathering fluxes increase on the Ethiopian Traps associated with El Niño conditions, but decrease on the southern part of the East African rift, they increase on the Andes near the equator, but decrease in the northernmost part of the range, and decrease on the central Himalaya but increase the western part. Hence, the anomaly of weathering flux integrated over those regions is close to zero (Fig. ??3c). Most of the negative anomaly of El Niño weathering comes from the Maritime Continent. The weathering integrated over this region is almost equal to the total anomaly (Fig. ??3c, purple bars). This result highlights the key role this area has potentially played in cooling Earth’s climate over the last few million years. The signal from the Maritime Continent is expanded by further a weathering decrease on the Deccan Traps and the Guiana highlands associated with El Niño conditions, and partially offset by an increase on the Brazilian highlands (Fig. 3and??).

It is interesting to note that although the sign of weathering anomalies under La Niña conditions is nearly everywhere the opposite of the ones under El Niño conditions, the magnitude of those anomalies is not perfectly symmetrical (Fig. ??3c).

### 3.2 Exploring the consequences of Pliocene SST

We wish here to take a step further and investigate the consequence of Pliocene-like gradients of SST on silicate weathering and equilibrium temperature (i.e., the global mean temperature for which silicate weathering balances degassing). We rely here on the work of ? demonstrating that the tropical zonal gradient of SST is linked to the meridional gradient of SST. This result indicates that Pliocene permanent El Niño could be a consequence of weakened meridional gradient. Drawing from their work, we designed climate simulations aimed at reproducing mimicking Pliocene SST, following the method of ?.

The climate simulations presented in ?, ?, and ? cannot be directly used because the simulations at  $0.9^\circ \times 1.25^\circ$  of resolution were only conducted at pre-industrial  $\text{CO}_2$ . However, estimating carbon cycle equilibrium with GEOCLIM necessitates climate simulations at several  $\text{CO}_2$  levels. This cannot be done with fixed SST simulations (such as from ?), because it will miss the warming of ocean surface with rising  $\text{CO}_2$ . On the other hand, changing atmospheric  $\text{CO}_2$  in a coupled ocean-atmosphere model at  $0.9^\circ \times 1.25^\circ$  would require a prohibiting computation time to let the full ocean be at equilibrium with the radiative forcing, and get the correct atmospheric warming. Another issue is that Burls and Fedorov (2014) produced their Pliocene-like SST pattern by altering the cloud properties in the cloud parameterization; as such, the physics of that simulation differs from that of the the pre-industrial control, and thus the two simulations are not directly comparable.

To overcome those difficulties, because of these constraints, we designed our simulations in 3 steps. First, we apply the method of ? to seek to reproduce Pliocene SST. In the slab ocean climate simulations that reproduce the Pliocene-like SST pattern of ?, simulations that can be run at many  $\text{CO}_2$  levels. We first followed the method of ? of altering the cloud radiative properties with a coupled ocean-atmosphere coupled version of CESM1.2, we modified the cloud visible albedo by changing the value of model. From those simulations, we generated a Q flux field that we used to force the slab ocean version of the climate model and reproduce the SST pattern of the water path in the radiative code of CAM4. The cloud liquid and solid water

path-multiplied-by-3.4 between North and South, and the cloud-liquid-water path-multiplied-by-0.4 in the rest of the Earth. We ran those simulations for 230 years, which is sufficient for the surface ocean to respond to the perturbation (?). At this point, we are not interested in accurately reaching the radiative equilibrium. The last 30 years of simulation were used to extract the SST field. This field exhibit the features of reduced zonal and meridional gradients, in accordance with ?. We refer to this SST field as the coupled ocean-atmosphere simulations. The generation of Q flux field implied conducting intermediate atmosphere-only simulations, this explained in details in Appendix B.

Two Q flux fields were actually generated, one for reproducing the entire SST pattern (“full Pliocene SST”)–We also ran a pre-industrial control simulation for 170 years, taking the last 30 years to extract the “pre-industrial control” SST field. In order to create a Pliocene SST field for the tropics only) and one for reproducing the SST pattern only between 10°S and 10°N (“10°SN Pliocene SST”), we merged the full Pliocene SST in the tropics to the pre-industrial control SST in the extratropics using

$$SST_{10SNPliocene} = fSST_{Pliocene} + (1 - f)SST_{Preindustrial}$$

where

$$f = \exp(-(latitude/10)^6)$$

with latitude in degrees.

Second, we took the pre-industrial control SST field, the Pliocene SST field, and the Pliocene SST field, ran fixed-SST simulations for each. Note that we use the standard CAM4 model for each simulation (i.e. we do not alter the cloud properties), so that the climate model physics is consistent. Those simulations were run at several levels (The motivation for isolating the SST pattern close to the equator is that El Niño events consist of the collapse of the tropical Pacific zonal gradient of SST, and for the full Pliocene SST; and for the Pliocene SST). We did so in order to estimate at which the atmosphere is in equilibrium with the SST, meaning that the net surface heat flux ( $F_{net}$ , Eq. B3) sums at zero. We estimated those levels as for the full Pliocene SST and for the Pliocene SST, by linearly interpolation  $F_{net}$  as a function of  $\log(CO_2)$ .  $F_{net}$  is computed as:

$$F_{net} = F_{SW} - F_{LW} - F_L - F_S$$

Where  $F_{SW}$  is the net (downward) solar flux,  $F_{LW}$  is net net (upward) long-wave flux,  $F_L$  is the latent heat flux, and  $F_S$  the sensible heat flux, all fluxes at Earth surface. These fixed-SST simulations were run 40 years, and the last 30 years were used to extract  $F_{net}$ . without major changes in extra-tropical SST patterns – though extra-tropical teleconnections do modify local SST – while Pliocene climate proxies indicate a reduction of both zonal and meridional gradients. Yet, El Niño is viewed as analogy for Pliocene climate, in particular, the same teleconnections are assumed to occur (?). Also, this configuration allows us to compare the effects of a permanent El Nino to that of the long-term average of transient El Ninos in section 3.1.2. Isolating the 10°S–10°N SST pattern allows us to investigate the teleconnections caused to the tropical part of the Pliocene SST estimate, without the effects of the reduced meridional gradient, to better compare it to El Niño events.

Third, we used 0-sum  $F_{net}$  from the full and Pliocene SST to derive oceanic Q flux:  $Q$ . The Q flux refers to the forcing term of a slab ocean model. It represents the divergence of oceanic heat transport, and directly controls the warming or cooling of

Anomaly of ocean skin temperature (i.e., SST, except on grid points with sea ice) for (a): fixed SST simulation with full Pliocene SST (at  $\tau$ ), (b): slab ocean simulation with full Pliocene SST (at  $\tau$ ), (c): fixed SST simulation with Pliocene SST (at  $\tau$ ), and (d): slab ocean simulation with Pliocene SST (at  $\tau$ ). Note that the scale in (a) and (b) is different from (c) and (d). Map projection and graticules are similar to Fig. ???. In (c), the temperature anomaly is exactly outside  $\pm 8^\circ\text{C}$ , except in polar regions because of the sea-ice surface temperature response to tropical SST forcing. In (d), the temperature anomaly is not perfectly outside  $\pm 3^\circ\text{C}$ , because of inaccuracies in the derivation of the Q flux, but the amplitude of those anomalies is significantly less than within  $10^\circ\text{S}$ – $10^\circ\text{N}$ , with the exception of sea-ice regions.

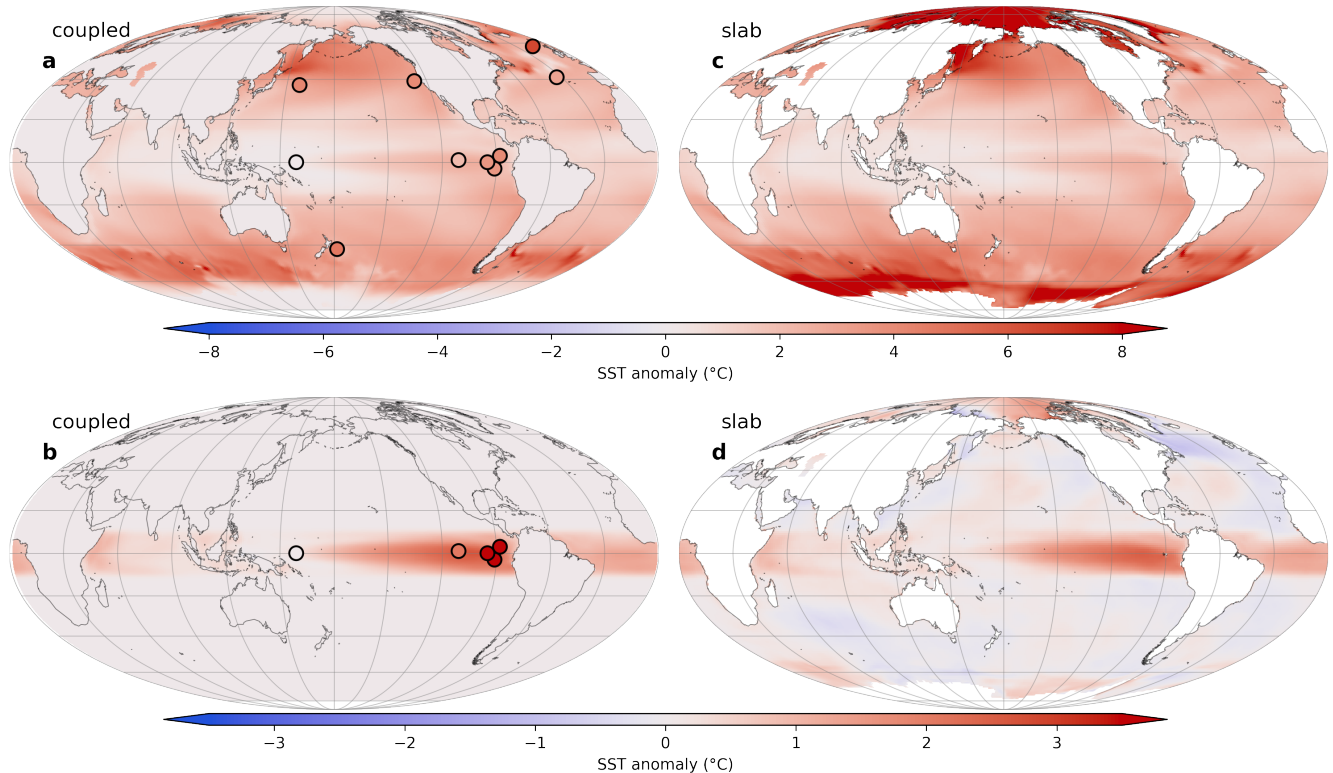


**Figure 4.** Anomaly of SST (a and b) and ocean skin temperature – i.e., SST, except on grid points with sea ice (c and d). (a): coupled ocean-atmosphere simulation with altered cloud properties (i.e. full Pliocene SST), pre-industrial  $\text{CO}_2$ , (b): same as (a) but SST anomaly field is truncated at  $10^\circ\text{N}$  or  $\text{S}$  (i.e.,  $10^\circ\text{SN}$  Pliocene SST). (c): slab ocean simulation with Q-flux derived to reproduce the full Pliocene SST (i.e., SST of panel a;  $\text{CO}_2$  at 300 ppmv). (d): slab ocean simulation with Q-flux derived to reproduce the  $10^\circ\text{SN}$  Pliocene SST (i.e., SST of panel b;  $\text{CO}_2$  at 299.4 ppmv). Note that the scale in (a) and (c) is different from (b) and (d). Colored dots in (a) and (b) are estimates of SST anomaly at 4.5–3.5 Ma from ODP proxies (see Appendix D). They follow the same colorscale than their underlying map. Map projection and graticules are similar to Fig. 1. Large temperature anomalies ( $> 8^\circ\text{C}$ ) in (c) are found in regions influenced by sea ice, and deviate from the original SST (panel a), that does not respond to the cloud albedo forcing (SST anomaly is  $0^\circ\text{C}$ ) because of the sea ice cover. Note that in (d), the temperature anomaly is not perfectly  $0^\circ\text{C}$  outside  $10^\circ\text{S}$ – $10^\circ\text{N}$ , because of inaccuracies in the derivation of the Q flux, but the amplitude of those anomalies is significantly less than within  $10^\circ\text{S}$ – $10^\circ\text{N}$ , with the exception of sea-ice regions.

the surface ocean, in a slab model. We computed the Q flux for each month of the annual cycle with the following equation:-

$$285 \quad Q(t) = F_{net}(t) - \rho_{wat} c_{p_{wat}} h_{ml} \frac{d(SST)}{dt} + \rho_{ice} L_{fus} h_{ice} \frac{dx_{ice}}{dt}$$

Where  $\rho_{wat}$  is the seawater density,  $c_{p_{wat}}$  is the seawater heat capacity,  $h_{ml}$  is the depth of ocean mixed layer,  $\rho_{ice}$  is the density of sea ice,  $L_{fus}$  is the latent heat of fusion of water,  $h_{ice}$  is the thickness of sea ice, and  $x_{ice}$  the fraction of each oceanic grid covered by sea ice. The time derivative was approximated here as the month by month finite difference. The mixed layer depth  $h_{ml}$  was taken from the default Figure 4 shows the comparison of the SST anomaly (with respect to pre-industrial Q flux forcing (see Methods, section 2.3) and is time-invariant. The SST and ice fraction ( $x_{ice}$ ) were control) taken from the Pliocene SST atmosphere-only simulations (full or coupled ocean-atmosphere simulations and the SST anomaly from the slab ocean simulations, for both the “full” and “10 °SN). More precisely, we computed the anomaly of  $SST$ ,  $x_{ice}$  and  $F_{net}$  by subtracting the fields taken from Pliocene SST atmosphere-only simulations to the fields from the pre-industrial control fixed-SST climate run. Noting this subtraction  $\Delta$ , we actually computed  $\Delta Q$  as:-

$$295 \quad \Delta Q(t) = \Delta F_{net}(t) - \rho_{wat} c_{p_{wat}} h_{ml} \frac{d(\Delta SST)}{dt} + \rho_{ice} L_{fus} h_{ice} \frac{d(\Delta x_{ice})}{dt}$$

With  $\Delta Q$  thus calculated, the Pliocene Q flux was computed as  $Q_{control} + \Delta Q$  (for both full SST or SST fields). Using this generated Q flux, we ran climate simulations with the slab ocean version of CESM1.2, at the “standard” level (or, see previous paragraph) cases. SST proxies from 10 ODP sites (see Appendix D) are also shown to Fig. 4 a and b. The comparison to the proxies confirm the results of ? that the alteration of clouds radiative properties reproduce the mid- and at higher or lower (high-latitude warming, , , and ) to encompass the full range of climate warming or cooling, and the Eastern tropical Pacific warming. This last warming, however, is not as pronounced (~ 2.5 °C) as must adjust to balance the geological cycle. Here again, the standard CAM4 model is used in all instances, so that the climate model physics is consistent, indicated by the proxies (~ 4 °C. See Fig. 4b).

The least constrained variable here is the sea-ice thickness ( $h_{ice}$ ). In the absence of information, as it cannot be retrieved from the fixed-SST simulations, we assumed a constant, uniform thickness of -. Despite this crude assumption, the The slab ocean simulations (at standard ) reproduce well the SST fields from the original ocean-atmosphere coupled model (see Fig. ??) patterns from the coupled ocean-atmosphere simulations, except in a few local spots, in regions influenced by sea-ice.

Finally, we note that these estimated levels that balance the heat flux in the fixed-SST simulations are different from the cycle equilibrium levels computed by GEOCLIM. The former is done so that the derived Q flux change does not artificially introduce heat into or out of the ocean. With a slab ocean model, For instance, on Fig. 4 b and d, it appears that the null  $F_{net}$  condition is verified for any level, because it is imposed by the Q flux. The latter levels computed by GEOCLIM are the ones that balance the geologic cycle “10 °SN Pliocene SST” slab ocean simulation fails to generate a strictly null SST anomaly outside the 10 °S–10 °N band, but the magnitude of those subtropical anomalies is negligible compared to the expected ones within 10 °S–10 °N. Regions influenced by sea-ice exhibit significant local differences, but they do not alter the global behaviour of the simulations.

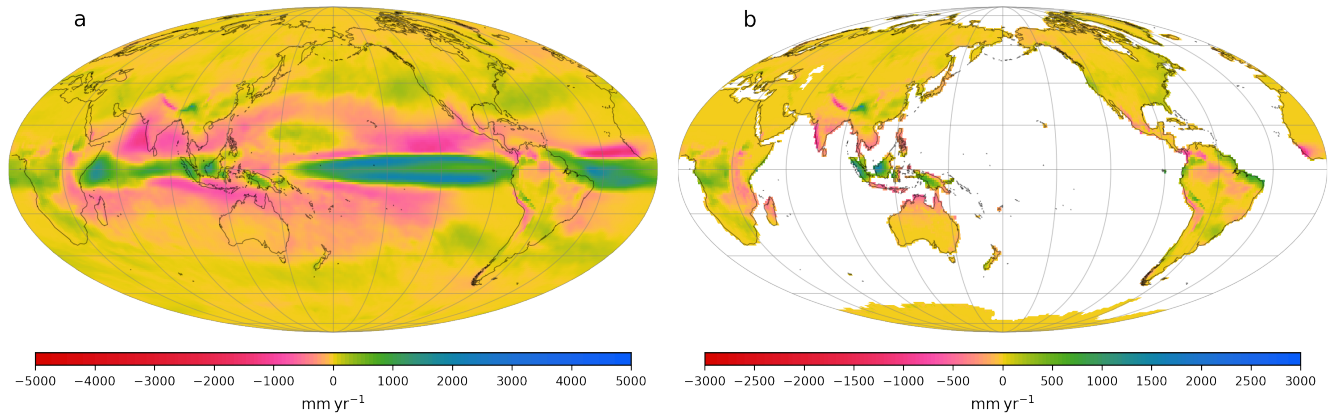


**Figure 5.** Annual mean climatology of slab ocean simulation with  $10^{\circ}\text{SN}$  Pliocene SST at 299.4 ppmv anomaly with respect to the pre-industrial control. (a): total precipitation, and (b): continental runoff. Map projection and graticules as in Fig. ??1. On each panel, non-significant differences are hatched ( $p$ -value of Welch's  $t$ -test  $> 0.1$ , see Appendix C)

### 3.2.1 Weathering and equilibrium temperature with reduced zonal gradient

In this section, we examine the simulations where the Pliocene SST field is applied in the  $10^{\circ}\text{S}$ – $10^{\circ}\text{N}$  band ( $10^{\circ}\text{SN}$  Pliocene SST) with the slab ocean version of CESM.

The standard  $\text{CO}_2$  experiment for this configuration (299.4 ppmv, see ~~previous section~~ Appendix B, section B2) has a  
 320 Global Mean 2 m Temperature of  $13.67^{\circ}\text{C}$ , which is  $0.25^{\circ}\text{C}$  warmer than the pre-industrial control (at 284.7 ppmv). The precipitation anomaly (Fig. 5a) exhibits a large increase in the eastern Pacific, similar to El Niño events. This increase does not extend southward as much as for observed El Niño conditions (Fig. ??1b), likely because we imposed SST perturbation only in the  $10^{\circ}\text{S}$ – $10^{\circ}\text{N}$  band. Instead of drier conditions around the Maritime Continent and wetter conditions in the western Indian ocean characteristic of El Niño, precipitation increases along the equator ( $\sim \pm 5^{\circ}$ ) across the Indian ocean, and extends up to  
 325 the eastern coast of Borneo over the Maritime Continent. The islands of Borneo, Sulawesi, and New Guinea show a similar pattern of wetter conditions except on their western edge. The tropical Atlantic also shows significant difference with El Niño, as because the imposed SST in the Atlantic is warmer almost uniformly along the equator (Fig. ??e-4 b and d), which favors atmospheric convection. The runoff anomaly (Fig. 5 a) reveals some similarities with the El Niño case (Fig. ??1c): a decrease over India and South-East Asia, an increase over China and the eastern side of the Himalaya, an increase in the Andes around  
 330 the equator, a decrease in the rest of equatorial South America (though the enhanced convection in the Atlantic generates wetter conditions along the Atlantic coast), an increase in the South-east part of South America, and an increase over the Congo basin. The largest discrepancies are found on the Maritime Continent, and the East African rift.

We then used the  $10^{\circ}\text{SN}$  Pliocene SST simulations at several  $\text{CO}_2$  levels to compute the equilibrium  $\text{CO}_2$ , which is the value at which the silicate weathering flux with  $10^{\circ}\text{SN}$  Pliocene SST balances  $\text{CO}_2$  degassing. More precisely, we consider  
 335 that control  $\text{CO}_2$  degassing is equal to pre-industrial silicate weathering flux. Therefore, for each selected combination of

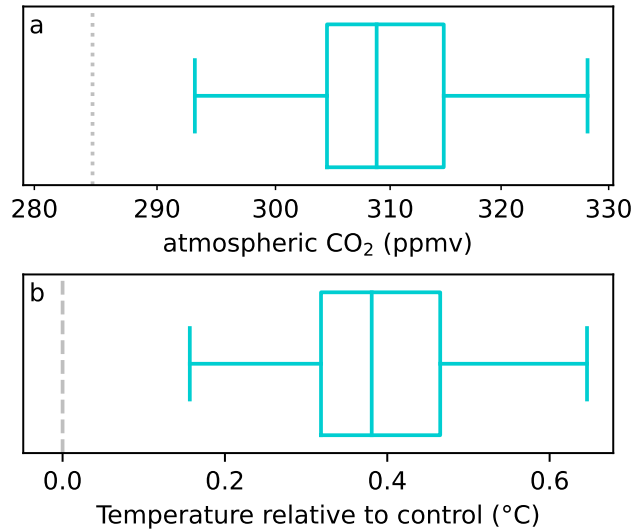


**Figure 6.** Results for the 10 °SN Pliocene SST GEOCLIM simulation at C cycle equilibrium (i.e., with silicate weathering flux balancing control degassing). (a): atmospheric CO<sub>2</sub> level (logarithmic axis) and (b): anomaly (with respect to pre-industrial simulation) of Global Mean 2 m Temperature. The anomaly in (b) is highlighted by a thin grey dotted-vertical line. The distribution – shown as a boxplot – represents the ensemble of GEOCLIM parameterizations (similarly to Fig. ??2c and ??3c). The x axis of panel (a) is bounded so that a given CO<sub>2</sub> in panel (a) correspond to the aligned global temperature in panel (b). This with the approximation that the CO<sub>2</sub> is continuously logarithmic (from lower to upper bound), whereas GEOCLIM log(CO<sub>2</sub>)-interpolates climate fields between the CO<sub>2</sub> levels – the ones considered here being 250 ppmv, 299.4 ppmv and 427.1 ppmv. Because of this approximation, the boxplots in (a) and (b) are not perfectly aligned, but this misalignment is negligible. The pre-industrial CO<sub>2</sub> level and the 0 °C anomaly are highlighted by the thin grey dashed or dotted vertical lines. Note that those two lines do not align because of the offset in the CO<sub>2</sub>-temperature relationship of the 10 °SN Pliocene SST simulation with respect to the pre-industrial one.

GEOCLIM parameters (see Methods, section 2.1), we imposed that the silicate weathering flux with 10 °SN Pliocene SST is equal to the silicate weathering flux with the same parameter combination in the pre-industrial control simulation (i.e., computed with climate fields from pre-industrial slab simulation. This “control” weathering is shown on Fig. ??2c, orange bars.) Figure 6 shows this equilibrium CO<sub>2</sub> (panel a) and the Global Mean 2 m Temperature corresponding to that CO<sub>2</sub> concentration (panel b). The Pliocene SST (within 10 °S–10 °N) generates climatic conditions less favourable for weathering, causing CO<sub>2</sub> to increase, and global temperature to rise by ~ 0.4 °C, which is about twice that estimated using ERA5 reanalysis of El Niño years. This result is consistent with the fact that, in the 10 °SN Pliocene SST simulation, the west-to-east Pacific SST difference is reduced by more (~ 2.5 °) than in the El Niño years climatology (~ 1.5 °). Note that, though the climate sensitivity (global temperature difference for a CO<sub>2</sub> doubling) stays the same, there is an offset in the CO<sub>2</sub>-temperature relationship, meaning that a CO<sub>2</sub> of 284.7 ppmv does not correspond to a 0 °C temperature anomaly -(see also Fig. 8a).

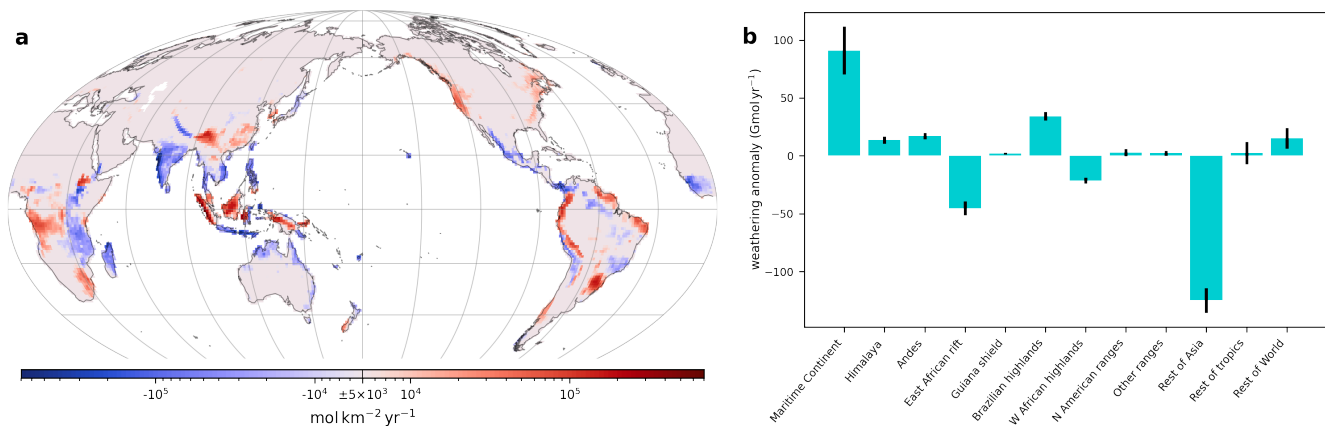


**Figure 7.** (a): Anomaly of weathering rate of slab ocean climate simulation with 10 °SN Pliocene SST at 299.4 ppmv with respect to pre-industrial control (averaged over the parameter combinations, similarly to Fig. 3). (b): Bar plot of the anomaly of weathering flux from panel (a) integrated over the geographic regions (similarly to Fig. 3c).

**Bar plot of the anomaly of weathering flux of slab ocean climate simulation with Pliocene SST at with respect to pre-industrial control, integrated over the geographic regions (similarly to Fig. ??).**

This decrease of weatherability (or weathering efficiency) can be investigated by looking at the anomaly of silicate weathering rate of 10 °SN Pliocene SST at 299.4 ppmv with respect to pre-industrial control weathering rate (Fig. 7). Though the global temperature is not the same (10 °SN Pliocene SST is 0.25 °C warmer), it still illustrates the causes of this decrease in weatherability. Similar to what was observed with El Niño and La Niña composites (Fig. 3), several positive and negative regional anomalies of weathering, driven by runoff changes, compensate each other, leading to a weak warming. Nevertheless, this warming is consistent over the whole ensemble of parameter combinations. Figure ??-7b show the integration of the weathering rate anomaly from Fig. 7a over the geographic regions presented Fig. ??2a. Unlike the El Niño case, the weathering anomaly integrated over the Maritime Continent is positive, and thereby not contributing to the warming. Indeed, there are more increases than decreases in runoff on the Maritime Continent in the 10 °SN Pliocene SST simulation. The East African rift also has an opposite behaviour, with a decrease of weathering instead of a slight increase with El Niño. The last main difference concerns the category “rest of Asia”, showing a large decrease in weathering. The decrease in runoff in India, and associated weathering decrease, overwhelms the increase in China, whereas those two balance out under modern El Niño conditions.

360 The weatherability decrease of the 10 °SN Pliocene SST simulation can also be appreciated by looking at the global temperature–total weathering flux relationship (Fig. 8b). The 10 °SN Pliocene SST curve (dashed blue) is systemically beneath the pre-industrial one (solid black), for any given global temperature. This means that regardless of the chosen background CO<sub>2</sub> degassing flux, the simulation with 10 °SN Pliocene SST will be warmer.

In summary, applying our estimation of Pliocene SST in the 10 °S–10 °N band – whose main feature is a flattening the tropical Pacific zonal gradient – generates a similar weatherability decrease and global warming to that estimated from El Niño

365



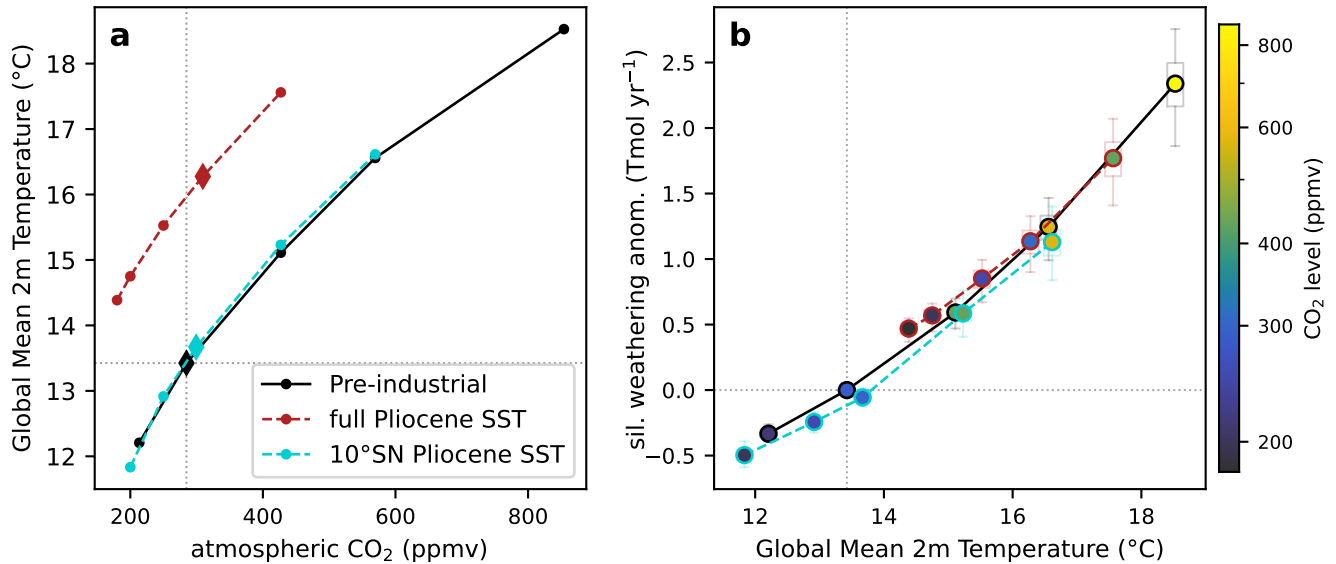


**Figure 8.** (a): Global Mean 2 m Temperature (GMST) plotted against atmospheric CO<sub>2</sub> level for the 3 series of slab ocean GCM simulations: pre-industrial boundary conditions, full Pliocene SST and 10°SN Pliocene SST. Each dot represents an actual simulation, the diamonds correspond to the “standard” CO<sub>2</sub> levels (284.7 ppmv for pre-industrial, see previous section for Pliocene SST). (b): Total silicate weathering fluxes anomaly (with respect to pre-industrial) plotted against GMST, for the same 3 series of slab ocean GCM simulations (same color code than panel a). Each circle represents a single simulation, at fixed CO<sub>2</sub>, its level and being indicated with the colorscale. The semi-transparent boxplots show, for each simulation, the variability of weathering across the parameter combinations. On each panel, null weathering anomaly, pre-industrial GMST and pre-industrial CO<sub>2</sub> level are highlighted by the horizontal and vertical thin grey dotted lines.

(section 3.1.2), though approximately twice as large. However, the mechanisms of that weatherability decrease are different, due to differences in the regional patterns of simulated runoff.

### 3.2.2 Simulation with full Pliocene Sea Surface Temperature

We now examine the slab ocean climate simulations where the full Pliocene SST field is applied. The most noticeable feature of the full Pliocene SST simulation is its mean temperature anomaly. As shown in Fig. 8a, for any given CO<sub>2</sub> level, the full Pliocene SST slab ocean simulation is about 2.5 °C warmer than its counterpart with pre-industrial boundary conditions.

These warmer conditions at a given CO<sub>2</sub> level can be explained by analysing the components of the radiative budget. Figure 9 shows the comparison between the full Pliocene SST simulation and pre-industrial simulations interpolated at 309.4 ppmv (same CO<sub>2</sub> level than as Pliocene SST simulation) and at 538.3 ppmv (CO<sub>2</sub> level at which the Global Mean 2 m Temperature equals the one of the Pliocene SST simulation). A significant signal of the full Pliocene SST simulation can be found in the net solar radiative flux at top of atmosphere (Fig. 9 a and e). There are 2 peaks of incoming radiation in the tropics (around

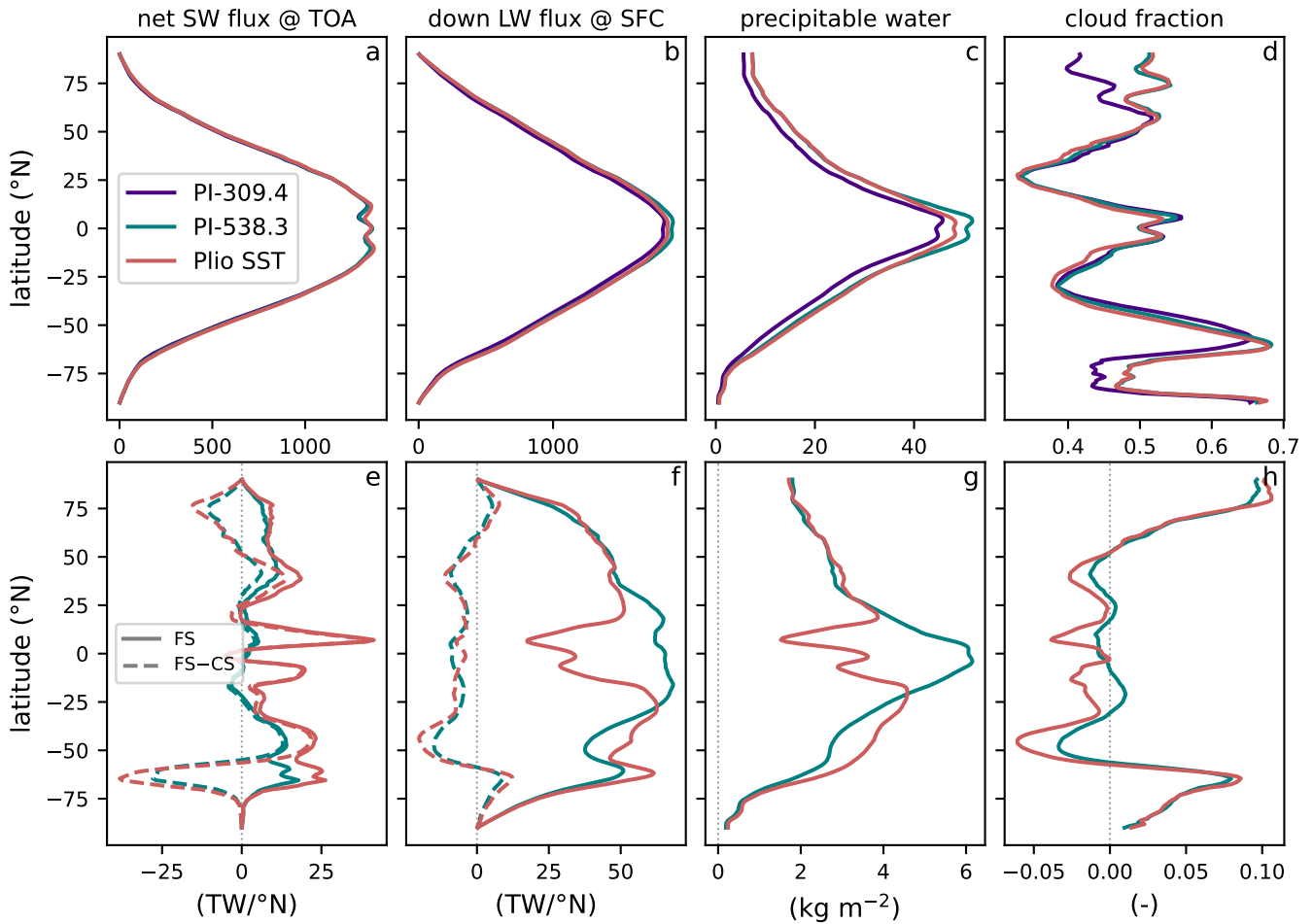


**Figure 9.** Comparison of zonal annual mean fluxes and climatology for the three simulations which are: pre-industrial boundary conditions  $\log(\text{CO}_2\text{-interpolated})$  at 309.4 ppmv (indigo) or at 538.3 ppmv (teal), and full Pliocene SST (at 309.4 ppmv). (a): zonally-integrated net (incoming minus outgoing) solar (SW) radiative flux at top of atmosphere (TOA), (b): zonally-integrated downwelling long-wave (LW) radiative flux at Earth surface (SFC), (c): zonally-averaged total precipitable water (vertically integrated), (d): zonally-averaged total cloud fraction (vertically integrated). All variables are annual mean climatology. (e), (f), (g) and (h) are similar to (a), (b), (c) and (d) (respectively) but with 309.4 ppmv pre-industrial subtracted, the thin vertical grey dashed line highlights zero anomaly. The dashed color lines in (e) and (f) shows the difference full sky (FS) minus clear sky (CS), illustrating the contribution from clouds. The solid lines (full sky) are the regular values, as in (a) and (b). The “0 anomaly” in panels (e)–(h) is highlighted by a thin grey dotted vertical line. The color code holds for the entire figure.

5°N and 10°S, Fig. 9e), that do not appear just by raising  $\text{CO}_2$  with pre-industrial boundary conditions. Such tropical peaks are caused by reduced cloudiness (Fig. 9 d and h), due to less intense convection because of the reduced zonal temperature gradient, lowering Earth visible shortwave albedo. Indeed, the cloud contribution to the peaks, estimated by the difference “full

380 sky” minus “clear sky” (dashed lines in Fig. 9e) is almost 100% of the signal. [The SST pattern effect on global cloud radiative feedback has indeed been recognized \(e.g., ?\)](#). Another peak in incoming solar radiation can be seen around 40 ° N or S Fig. (9e) and corresponds to a poleward shift in cloudiness at those latitudes (Fig. 9d), mostly discernable in the Southern Hemisphere. This feature, however, is also found in the pre-industrial simulation at 538.3 ppmv, and may be a mere consequence of rising global temperature, though its amplitude is higher in the full Pliocene SST simulation. More solar radiation also enters at  
385 high latitude in the Pliocene simulations relative to the pre-industrial control, due to the retreat of sea ice, also lowering [visible shortwave](#) albedo. Though it is countered by increase in cloudiness (Fig. 9d and h), as can be seen in the cloud contribution in Fig. 9e, the net effect is still positive. Similarly to the peak at 40 ° N or S, this phenomenon is also present in the pre-industrial 538.3 ppmv simulation, but strengthened in the Pliocene SST simulation. On global average, the net solar radiation forcing of the full Pliocene simulation (with respect to pre-industrial at same CO<sub>2</sub>) is +3.9 W m<sup>-2</sup>, the tropical part alone being +1.0  
390 equivalent W m<sup>-2</sup> (equivalent if spread on the whole Earth). The latitude profile of downwelling long-wave radiation at Earth surface also shows some variations (Fig. 9 b and f), essentially following the anomaly of water vapour (Fig. 9 c and g). The reduced meridional temperature gradient in the full Pliocene SST simulation is responsible for less water vapour in the tropics, and more water vapour in the extra-tropics, compared to the pre-industrial simulation at same mean temperature (Fig. 9g), though it is mostly visible in the Southern hemisphere. The downwelling long-wave radiation at the surface exhibits the same  
395 behaviour. The more significant drops in the tropics (still compared to the pre-industrial simulation at same mean temperature) is likely due to the reduced Hadley circulation. The averaged downwelling long-wave flux anomaly is not so different between the Pliocene SST simulation and the pre-industrial one at 538.3 ppmv (respectively, +14.0 and +15.8 W m<sup>-2</sup>), both seem to be a consequence of warmer atmosphere (and amplifier, through a positive feedback loop). In summary, we can conclude that the main warming causes of the full Pliocene SST simulation are the decrease in cloudiness in the tropics, due to a weaker  
400 convection and Hadley circulation, combined with a decrease of cloudiness around 40 ° N and S and of sea ice at high latitude, these last two also being part of a positive feedback enhancing the “initial” warming.

In term of precipitation, it is easier to compare the full Pliocene SST simulation with the pre-industrial simulation log(CO<sub>2</sub>)-interpolated at the same global temperature, to cancel the effect of increased precipitation with global warming. This precipitation (and runoff) difference is shown on Fig. 10. A redistribution of precipitation, with a decrease in the tropics and an increase  
405 in the extra-tropics can be observed, superimposed to the anomalies already observed in the 10 °SN Pliocene SST simulation (Fig. 5): increase in the eastern tropical Pacific and on the western boundaries of tropical Indian and Atlantic oceans. The results are different for land precipitation. Despite the reduced meridional temperature gradient, precipitation and runoff mostly increase in tropical Africa and South America, with the exception of the western part of this Amazon basin and the East African rift, where a drying tendency was already observed in the 10 °SN Pliocene SST simulation. This goes against our  
410 initial hypothesis, based on the “wet gets dryer, dry gets wetter” feature from ?. The Maritime Continent exhibits a contrasting behaviour, with wetter conditions on the western sides of the most equatorial islands, and dryer conditions on their eastern side. Such behaviour was also present in the 10 °SN Pliocene SST simulation, with a larger precipitation increase on the western sides, but is highlighted here because the anomaly is computed with respect to the pre-industrial simulation at 538.3 ppmv instead of 284.7 ppmv: the increase on the eastern sides is less than the roughly uniform increase due to higher CO<sub>2</sub>, whereas

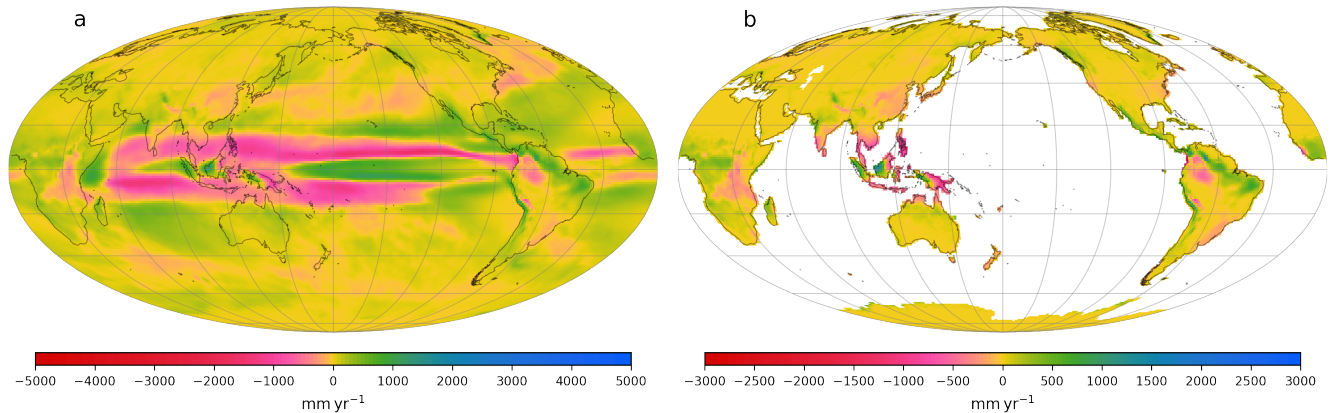


**Figure 10.** Annual mean climatology of the slab ocean simulation with full Pliocene SST at 309.4 ppmv with respect to the pre-industrial control  $\log(\text{CO}_2)$ -interpolated at 358.3 ppmv. This last  $\text{CO}_2$  level was chosen so that the two simulations in the difference have the same Global Mean 2 m Temperature. (a): total precipitation, and (b): continental runoff. Map projection and graticules as in Fig. ??1. On each panel, non-significant differences are hatched (p-value of Welch's t-test > 0.1, see Appendix C)

415 the increase on the western sides is larger. On global average, precipitation increase by  $15 \text{ mm yr}^{-1}$  and continental runoff increase by  $16 \text{ mm yr}^{-1}$ .

~~Total silicate weathering fluxes anomaly (with respect to pre-industrial control) plotted against Global Mean Temperature (GMST), for the pre-industrial and the full Pliocene SST simulations (each of those repeated at 5 different levels, see also Table B1). Each dot represents a single simulation, at fixed, its level being indicated with the color scale. The semi-transparent boxplots show, for each simulation, the variability of weathering across the parameter combinations. Null weathering anomaly and pre-industrial GMST are highlighted by the vertical and horizontal thin grey dotted lines.~~

420

The offset in global temperature for a given  $\text{CO}_2$  level (in full Pliocene SST simulations, with respect to pre-industrial ones) poses a technical problem: to go back down to pre-industrial temperature, with full Pliocene SST,  $\text{CO}_2$  needs to be lowered to  $\sim 140 \text{ ppmv}$ . Such  $\text{CO}_2$  levels are unrealistically low and are even lower than those during Pleistocene glacial maxima.

425 Moreover, at this  $\text{CO}_2$  level, plant stomates cease to operate normally in the land model of CESM, with huge consequences on the hydrologic cycle. Shut stomates behaviour contrasts with the regular tendency for stomates is to be more open at lower  $\text{CO}_2$  and severely reduces transpiration, eventually leading to increased global runoff, though the mean temperature is lower. Therefore, it is not possible to properly simulate silicate weathering with GEOCLIM. Increased runoff would lead to increased weathering at lower  $\text{CO}_2$  (thereby killing the negative feedback); ~~on~~. This effect is likely responsible of the “flattening” of the temperature-weathering curve at the lowest tested  $\text{CO}_2$  levels (dashed red curve on Fig. 8b). On the other hand, the fact that

430 plants cannot survive would undermine weathering, as plant roots are a major weathering agent. One may expect this second effect to be stronger, and hence to see a collapse of total weathering flux with even lower  $\text{CO}_2$ . For this reason, we cannot perform the inversion to compute the equilibrium  $\text{CO}_2$  where silicate weathering flux balances pre-industrial degassing. We instead analyse the weathering fluxes at fixed  $\text{CO}_2$ .

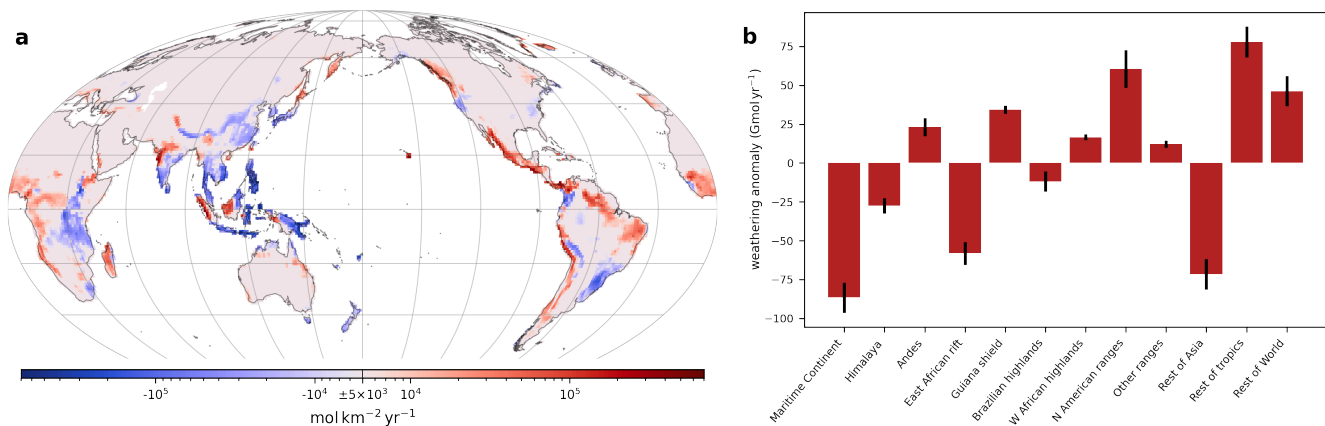


**Figure 11.** Similar to Fig. 7, anomaly (a): Anomaly of weathering rate of slab ocean climate simulation with full Pliocene SST at 309.4 ppmv. The anomaly is computed with respect to pre-industrial simulation interpolated at 358.3 ppmv (see Fig. 10); (b): Bar plot of the anomaly of weathering flux from panel (a).

435 Bar plot of the anomaly of weathering flux of the slab ocean climate simulation with full Pliocene SST at with respect to pre-industrial control interpolated at (see text and Fig. 10, and integrated over the geographic regions (similarly to Fig. ??).

Figure ?? shows Figure 8b illustrates the silicate weathering fluxes of the pre-industrial (solid black curve) and full Pliocene SST (dashed red curve) simulations. Despite the higher continental runoff, compared to the pre-industrial simulation at the same global temperature, the full Pliocene SST temperature-weathering curve and the pre-industrial curve are superimposed, except for very low CO<sub>2</sub> (< 200 ppmv) Pliocene simulations. This result means that Pliocene SST does not generate any significant increase or decrease of weatherability, save perhaps – except at low CO<sub>2</sub>, which is but likely due to CO<sub>2</sub>-plants interaction – if and stomates closure that generates higher runoff. If the carbon cycle was left to reach balance, with pre-industrial degassing, CO<sub>2</sub> would decrease until temperature is back around pre-industrial one, although that temperature value is hard to estimate given the uncertainties on weathering at low, but it is not possible to determine what would be the equilibrium temperature. The dashed red curves on Fig. 8b cannot be extrapolated on the lower bound because it will falls outside range of validity of the weathering model.

The fact that higher mean runoff does not lead to higher weatherability means that the regions where runoff decrease matter more in term of weathering. Comparing the full Pliocene SST simulation to the pre-industrial interpolated at the same global temperature (358.3 ppmv) reveals weathering decreases in the almost all of the South-East Asia, India, China, the East African rift, and even the Brazilian highlands and the Himalaya (Fig. 11). The combined decrease of those regions – mostly the first 4 four – is enough to counteract the increase in rest-of-the-rest of the tropical land masses (Africa and South America), and along most the-of-of the American Cordillera (from the Andes to the Cascade range, Fig. 11a) as shown in Figure ??- Fig. 11b.

## 4 Discussion

Our results emphasize the different effects on silicate weathering of meridional and tropical zonal ~~gradient-of-temperature~~  
455 ~~temperature gradients~~, that are characteristic of Pliocene warmth, according to temperature proxies and mechanistic connection  
between meridional and zonal SST gradients (?).

An estimate of the consequences of Pliocene permanent El Niño using reanalysis of modern El Niño events suggests a  
reduction of global weatherability by 1.7%, that would correspond to a  $\sim 0.23^\circ\text{C}$  warming ~~relative to today~~ (assuming a  
simple linear weathering ~~sensitivity feedback of~~  $\sim 0.4 \text{ Tmol yr}^{-1}$  ~~per~~  $^\circ\text{C}$  ~~of global warming by~~  $\text{CO}_2$  ~~that compensates the~~  
460 ~~+1.7% weathering anomaly~~). Climate simulations with ~~an-estimated-a~~ ~~“permanent El Niño”~~ reconstruction of Pliocene SST  
in the  $10^\circ\text{S}$ – $10^\circ\text{N}$  band indicate a  $\sim 0.4^\circ\text{C}$  warming relative to present-day conditions, but arising from different mecha-  
nisms. While El Niño reanalysis emphasized the role of the Maritime Continent in this warming ~~through reduced weathering~~  
~~flux fluxes~~, climate simulations suggest in contrast ~~a~~ higher weathering flux in the Maritime Continent, offsetting the warm-  
ing generated by ~~the~~ weathering decrease in mainland South-East Asia, India and the East African rift. Determining which  
465 of the two scenarios is the most reliable is not an easy task. Climate models contain biases, in particular for simulating pre-  
cipitation. The way precipitation on the Maritime Continent is affected by SST changes, in the CESM model, may not be  
accurate. ~~One potential cause could be the poorly simulated diurnal cycle in atmospheric convection on those islands. Indeed,~~  
~~the fully-coupled version of the climate model we used simulates rainfall increases in the winter and spring months over the~~  
~~South East Asian Islands following peak El Niño, unlike the weak drying seen in observations (Deser et al. 2012, compare~~  
470 ~~their figures 9 and 10)~~. On the other hand, modern El Niño ~~are transient events, lasting a few months, consists of transient~~  
~~events evolving over a period of a year and~~ with a peak in winter, and not subject to the constraint of balancing ~~the Earth~~Earth’s  
radiative budget. These features differ from stationary (permanent) El Niño conditions. ~~There is no guarantee that, where~~  
~~the anomalously warm SSTs over the eastern equatorial Pacific occur for all months. Thus, modern-day~~ El Niño events ~~are a~~  
~~perfect analog of and their teleconnected impacts are likely to be quite different from that of a~~ Pliocene permanent El Niño.  
475 ~~Differences in tropical climate dynamics need to be consider in particular as we found significant differences between El Niño~~  
~~reanalysis and our Pliocene SST experiments.~~

Nonetheless, the results agree on a ~~moderate warming effect~~ ~~modest warming effect~~ ( $\sim 0.4^\circ\text{C}$ ) of permanent El Niño  
resulting from ~~a~~ reduced global weatherability ~~relative to the present day. Though its amplitude is small, this warming is~~  
~~robust across all weathering model parameterizations~~. However, this effect is not seen when the entire estimation of Pliocene  
480 SST is applied to the climate model. Further complications arise from the radiative budget of the Pliocene SST simulation ~~;~~  
that is  $\sim 2.5^\circ\text{C}$  ~~warmer~~ than pre-industrial for a given  $\text{CO}_2$  level. This temperature shift is mostly caused by lower ~~visible~~  
~~shortwave~~ albedo due to fewer clouds in the tropics, as well as a poleward shift in the mid-latitude peak of cloudiness, and  
reduced sea-ice. If ~~a~~ flatter meridional temperature gradient is the result of ~~higher warmer~~ global temperature (due to higher  
 $\text{CO}_2$ ), a direct consequence would be that climate sensitivity to  $\text{CO}_2$  is much higher than current ~~estimations. This raise~~  
485 ~~estimates. This raises~~ the question of how representative of Pliocene SST is our reconstruction using ?’s method – modifying  
clouds ~~visible albedo~~ ~~shortwave albedo~~ – ~~though it is globally in agreement with SST proxies~~.

~~Overall, counteracting regional increase and decrease of land precipitation tends to balance.~~ The larger lesson we learn from our simulations is that SST pattern changes result in large regional changes in weathering of both signs. They tend to cancel each other out ~~in a permanent El Niño, though uncertainties remain on the overall net effect. Additionally, the,~~ but depending on the SST pattern there can still be a significant warming effect, as seen in the permanent El Niño and 10°S–10°N Pliocene SST cases. While the effect of reduced meridional SST gradient seems to cancel the ~~warming potential of~~ reduced tropical zonal SST gradient ~~in our Pliocene SST simulation~~ by increasing mean precipitation and continental runoff, ~~and no significant weatherability decrease due to dryer tropics is observed.~~ this cancellation could be seen as fortuitous and that (say) a different magnitude of the reduced meridional SST gradient could give rise to a net effect. A proper evaluation of the weatherability pattern effect for the Pliocene thus requires a robust SST reconstruction for that time period.

## 5 Conclusions

Long-term cooling of Earth's climate from the mid-Miocene to the present associated with decreasing CO<sub>2</sub> likely resulted from ~~increase~~ increased weatherability (e.g., ?), ~~decrease outgassing (e.g., ?)~~ decreased outgassing (e.g., ?, though no clear change is noted since , or a combination of the two. Superimposed on this long-term trend are large changes in climate dynamics whose ~~impact~~ impacts on regional climatology could ~~play~~ play an important role in processes such as the growth of Northern Hemisphere ice sheets (e.g., ?). Additionally, regional changes in precipitation and runoff could alter silicate weathering with resulting implications for geologic carbon sequestration and steady-state CO<sub>2</sub> levels. ~~This phenomenon can be called~~ We coin this phenomenon the “weatherability pattern effect”, ~~by analogy with~~ analogous to the pattern effect in climate sensitivity. In this contribution, we investigated the “weatherability pattern effect” due to SST gradients. We both put forward and evaluate the hypothesis that the transition from a Pliocene permanent El Niño climate to a modern El Niño-Southern Oscillation climate could be associated with an increase in weatherability due to ~~increases in runoff in~~ shifts in precipitation to or from chemical weathering hotspots. We ~~find support for this hypothesis through running chemical weathering models utilizing~~ explored this hypothesis by running a chemical weathering model with El Niño climate as ~~found~~ in reanalysis data ~~and through imposing tropical Pliocene SST— with complexities emerging in seeking to utilize a full Pliocene SST boundary condition.~~ Overall, ~~the difference of a permanent El Niño climate state on global silicate weathering and resulting simulated differences in global temperature are relatively minor given compensating regions of enhanced versus diminished chemical weathering. Significant differences are,~~ and by climate model simulations imposing Pliocene-like SST changes. Significant regional changes of both signs are found in the weathering patterns of the different experiments, particularly ~~on~~ in tropical weathering hotspots. These changes largely cancel, but can produce a modest but significant weatherability increase should they not entirely compensate. These results highlight the ~~importance and the uncertainties of tropical climate and associated dynamics~~ potential importance of the weatherability pattern effect on Earth's long-term ~~climate cycle~~ carbon cycle, though a proper evaluation requires a robust reconstruction of the relevant SST patterns.

*Code availability.* All code associated with this study can be found on Github (<https://github.com/piermafrost/GEOCLIM-dynsoil-steady-state/tree/PEN>) that is also archived on Zenodo (generate archive at time of revisions)

520 *Data availability.* All climate and GEOCLIM simulations used for this study are available on the dataset <https://doi.org/10.6078/D11H7D>

### **Appendix A: Calculation of ENSO index in ERA5 reanalysis**

We generated the ENSO index from the climate fields from ERA5 reanalysis (1979–2020 time-series) as follows: we used the detrended monthly SST average on Niño 3 region, that is  $5^{\circ}\text{N}$ – $5^{\circ}\text{S}$ ,  $150^{\circ}$ – $90^{\circ}\text{W}$  (?). We detrended the time-series by performing a linear regression with respect to time, and subtracted the “time” term from the original time-series. We grouped the monthly time-series in “year” vectors of 12 elements, corresponding to the 12 months, from May to April of the next calendar year. We subtracted to each year vector the average of all years, to center the vectorial time-series. We then performed a principal component analysis. We identified the first eigenvector (or EOF, for empirical orthogonal function) as the signature of El Niño events. We projected the detrended, centered, vectorial time-series on this first EOF (scalar product of the two 12 elements vectors, for each year). We normalized the scalar time-series obtained in this way by dividing it by its standard deviation (across the years). This normalized time-series can be interpreted as a time-series of the El Niño index for each year. We selected the El Niño years as the years having an index  $> 0.9$ , and  $< -0.9$  for the La Niña years.

525

530

The resulting ENSO index yearly time-series is shown in Fig. A1.

### **Appendix B: Design of slab ocean simulations with Pliocene SST**

The aim of the following procedure is to generate slab ocean climate simulations – at several  $\text{CO}_2$  levels – with SST patterns that replicate the meridional and tropical zonal gradients presented in ????. We proceeded in three steps.

535

#### **B1 Full ocean simulations at pre-industrial $\text{CO}_2$**

For this step, we strictly applied the method of ? to seek to reproduce Pliocene SST. From this simulation, we will only consider the SST field.

540

In the ocean-atmosphere coupled version of CESM1.2, we modified the cloud shortwave albedo by changing the value of the water path in the radiative code of CAM4. The cloud liquid and solid water path multiplied by 3.4 between  $15^{\circ}\text{N}$  North and South, and the cloud liquid water path multiplied by 0.4 for the rest of the Earth. We ran those simulations for 230 years, which is sufficient for the surface ocean to respond to the perturbation (?). At this point, we are not interested in accurately reaching the radiative equilibrium. The last 30 years of simulation were used to extract the SST field. This field exhibits the features of reduced zonal and meridional gradients, in accordance with ?. We refer to this SST field as the “full Pliocene SST”.

545

We also ran a pre-industrial control simulation for 170 years, taking the last 30 years to extract the “pre-industrial control” SST



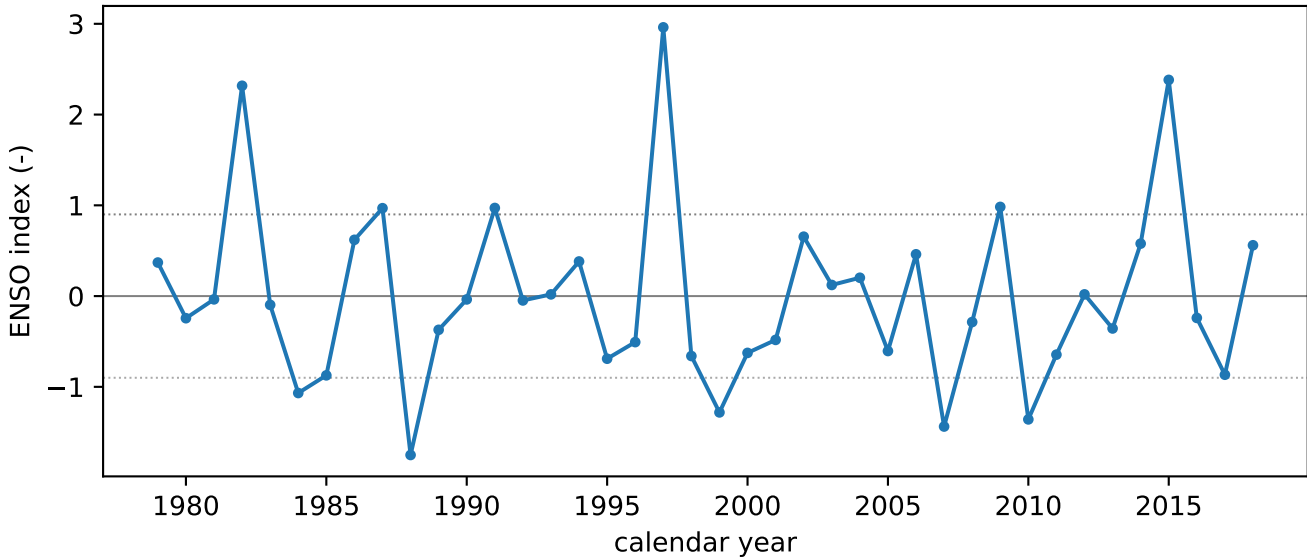


**Figure A1.** Time-series of the calculated ENSO index. The horizontal lines highlight the 0 value and the thresholds values of 0.9 and -0.9 chosen for El Niño and La Niña years respectively.

field. Finally, in order to create a Pliocene SST field for the tropics only, we merged the full Pliocene SST in the tropics to the pre-industrial control SST in the extratropics using

$$SST_{10SN Pliocene} = f SST_{Pliocene} + (1 - f) SST_{Preindustrial} \quad (B1)$$

where

$$f = \exp(-(latitude/10)^6) \quad (B2)$$

with latitude in degrees. We refer to this SST field as the “10 °SN Pliocene SST”

## B2 Fixed-SST simulations with zero-integral net ocean-atmosphere heat flux

In this second step, we took the “pre-industrial control SST”, the “full Pliocene SST”, and the “10 °SN Pliocene SST” fields, and ran atmosphere-only (i.e., fixed-SST) simulations for each of those fields.

Note that we use the standard CAM4 model for each simulation (i.e. we do not alter the cloud properties), so that the climate model physics is consistent. Those simulations were run at several CO<sub>2</sub> levels (284.7 ppmv, 300 ppmv and 320 ppmv for the full Pliocene SST; 284.7 ppmv and 300 ppmv for the 10 °SN Pliocene SST). We did so in order to estimate at which CO<sub>2</sub> the atmosphere is in equilibrium with the SST, meaning that the net surface heat flux ( $F_{net}$ , Eq. B3) sums at zero. We estimated those CO<sub>2</sub> levels as 309.4 ppmv for the full Pliocene SST and 299.4 ppmv for the 10 °SN Pliocene SST, by linearly

560 interpolation  $F_{net}$  as a function of  $\log(\text{CO}_2)$ .  $F_{net}$  is computed as:

$$F_{net} = F_{SW} - F_{LW} - F_L - F_S \quad (\text{B3})$$

Where  $F_{SW}$  is the net (downward) solar flux,  $F_{LW}$  is net (upward) long-wave flux,  $F_L$  is the latent heat flux, and  $F_S$  the sensible heat flux, all fluxes at Earth surface. These atmosphere-only simulations were run 40 years, and the last 30 years were used to extract  $F_{net}$ .

### 565 **B3 Slab ocean simulations with Pliocene SST**

In this last step, we used 0-sum  $F_{net}$  from the “full” and “10 °SN Pliocene SST” atmosphere-only simulations to derive oceanic Q flux:  $Q$ . The Q flux refers to the forcing term of a slab ocean model. It represents the divergence of oceanic heat transport, and directly controls the warming or cooling of the surface ocean, in a slab model.

We computed the Q flux for each month of the annual cycle with the following equation:

$$570 \quad Q(t) = F_{net}(t) - \rho_{wat} c_{pwat} h_{ml} \frac{d(SST)}{dt} + \rho_{ice} L_{fus} h_{ice} \frac{dx_{ice}}{dt} \quad (\text{B4})$$

Where  $\rho_{wat}$  is the seawater density,  $c_{pwat}$  is the seawater heat capacity,  $h_{ml}$  is the depth of ocean mixed layer,  $\rho_{ice}$  is the density of sea ice,  $L_{fus}$  is the latent heat of fusion of water,  $h_{ice}$  is the thickness of sea ice, and  $x_{ice}$  the fraction of each oceanic grid covered by sea ice. The time derivative was approximated here as the month by month finite difference. The mixed layer depth  $h_{ml}$  was taken from the default pre-industrial Q flux forcing (see Methods, section 2.3) and is time-invariant. The SST and ice  
 575 fraction ( $x_{ice}$ ) were taken from the Pliocene SST atmosphere-only simulations (full or 10 °SN).

More precisely, we computed the anomaly of  $SST$ ,  $x_{ice}$  and  $F_{net}$  by subtracting the fields taken from Pliocene SST atmosphere-only simulations to the fields from the pre-industrial control atmosphere-only climate run. Noting this subtraction  $\Delta$ , we actually computed  $\Delta Q$  as:

$$\Delta Q(t) = \Delta F_{net}(t) - \rho_{wat} c_{pwat} h_{ml} \frac{d(\Delta SST)}{dt} + \rho_{ice} L_{fus} h_{ice} \frac{d(\Delta x_{ice})}{dt} \quad (\text{B5})$$

580 With  $\Delta Q$  thus calculated, the Pliocene Q flux was computed as  $Q_{control} + \Delta Q$  (for both full SST or 10 °N/S SST fields). Using this generated Q flux, we ran climate simulations with the slab ocean version of CESM1.2, at the “standard”  $\text{CO}_2$  level (309.4 ppmv or 299.4 ppmv, see previous paragraph) and at higher or lower  $\text{CO}_2$  (180 ppmv, 200 ppmv, 250 ppmv, 427.1 ppmv and 569.4 ppmv) to encompass the full range of climate warming or cooling, as  $\text{CO}_2$  must adjust to balance the geological C cycle. Here again, the standard CAM4 model is used in all instances, so that the climate model physics is  
 585 consistent.

The least constrained variable here is the sea-ice thickness ( $h_{ice}$ ). In the absence of information, as it cannot be retrieved from the atmosphere-only simulations, we assumed a constant, uniform thickness of 1 m. Despite this crude assumption, the slab ocean simulations (at standard  $\text{CO}_2$ ) reproduce well the SST fields from the original ocean-atmosphere coupled model (see Fig. 4).

**Table B1.** Summary of all the climate simulations used for the present study (including “intermediate” simulations) and the specificity of their design.

<u>Name</u>	<u>boundary conditions*</u>	<u>ocean model</u>	<u>CO<sub>2</sub> level (ppmv)</u>	<u>integration time</u>
<u>COA-ctrl</u>	<u>pre-industrial</u>	<u>full</u>	284.7	170 yr
<u>COA-Plio</u>	<u>modified cloud albedo</u>	<u>full</u>	284.7	230 yr
<u>fSST-ctrl</u>	<u>pre-industrial</u>	<u>fixed SST</u>	284.7	40 yr
<u>fSST-Plio-full</u>	<u>SST from “COA-Plio”</u>	<u>fixed SST</u>	284.7; 300; 320	40 yr
<u>fSST-Plio-10SN</u>	<u>10 °S–10 °N SST from “COA-Plio”</u>	<u>fixed SST</u>	284.7; 300	40 yr
<u>control</u>	<u>pre-industrial</u>	<u>slab</u>	213.5; 284.7; 427.1 569.4; 854.1; 1138.8	50 yr
<u>full Pliocene SST</u>	<u>Q flux derived from “fSST-Plio-full”</u>	<u>slab</u>	180; 200; 250 309.4; 427.1	50 yr
<u>10°SN Pliocene SST</u>	<u>Q flux derived from “fSST-Plio-10SN”</u>	<u>slab</u>	200; 250; 299.4 569.4; 854.1	50 yr

\* refers to all climate model boundary conditions except atmospheric CO<sub>2</sub>. Anything else than the indicated modifications is pre-industrial

590 We note that these estimated CO<sub>2</sub> levels that balance the heat flux in the atmosphere-only simulations are different from the C cycle equilibrium CO<sub>2</sub> levels computed by GEOCLIM. The former is done so that the derived Q-flux change does not artificially introduce heat into or out of the ocean. With a slab ocean model, the null  $F_{net}$  condition is verified for any CO<sub>2</sub> level, because it is imposed by the Q flux. The latter CO<sub>2</sub> levels computed by GEOCLIM are the ones that balance the geologic C cycle.

595 Finally, we ran “full Pliocene SST” and “10 °N/S Pliocene SST” slab ocean simulations at several CO<sub>2</sub> levels using the Q fluxes thus generated. Table B1 summarizes all the climate simulations that were conducted for this study. The slab ocean simulations (last two entries of Table B1) are the main focus of the article, the other simulations are intermediate simulations needed to design the slab ocean simulations.

### **Appendix C: Statistical significance tests**

600 Figures 1, 5 and 10 include statistical tests to determine statistically significant patterns in the anomalies. In every case, a Welch’s t-test was performed, to compare the “control” and the “perturbed” fields (temperature, precipitation or runoff). For those tests, we considered samples of annual means (i.e., 1-year average), where every year is assumed to be an independent observation. Hence, the variance estimates used for the tests are the empirical variance between the years. The null hypothesis of the test is that the “control” and “perturbed” averages (i.e., average of all the 1-year annual means) are equal.

**Table D1.** Details of SST proxies shown in the present study

<u>ODP site</u>	<u>longitude</u>	<u>latitude</u>	<u>averaging interval</u>	<u>paleo SST</u>	<u>modern SST</u>	<u>reference</u>
<u>1125</u>	-178 °E	-42 °N	3.536 Ma – 4.485 Ma	19.74 °C	15 °C	<u>?</u>
<u>850</u>	-111 °E	1 °N	3.73 Ma – 4.33 Ma	26.97 °C	24.9 °C	<u>?</u>
<u>806</u>	159 °E	0 °N	3.54 Ma – 4.44 Ma	28.2 °C	28.2 °C*	<u>?</u>
<u>1208</u>	158 °E	37 °N	3.52 Ma – 4.49 Ma	21.72 °C	17.5 °C	<u>?</u>
<u>1021</u>	-128 °E	39 °N	3.53 Ma – 4.48 Ma	15.01 °C	11 °C*	<u>?</u>
<u>607</u>	-33 °E	41 °N	3.9 Ma – 4.1 Ma	21.5 °C	18.5 °C	<u>?</u>
<u>846</u>	-91 °E	-3 °N	4.0 Ma – 4.3 Ma	27 °C	23.5 °C	<u>?</u>
<u>847</u>	-95 °E	0 °N	4.0 Ma – 4.3 Ma	28 °C	24.5 °C	<u>?</u>
<u>982</u>	-16 °E	58 °N	3.9 Ma – 4.1 Ma	17.5 °C	11 °C	<u>?</u>
<u>1241</u>	-88 °E	3 °N	4.0 Ma – 4.3 Ma	28.5 °C	24.5 °C	<u>?</u>

\* taken from the SST proxy time-series (see text)

605 For the CESM simulations, the “control” population is the 30-year climatology of the pre-industrial simulation, and the “perturbed” populations are the 30-year climatology of either the 10 °SN Pliocene SST (Fig. 5) or full Pliocene SST (Fig. 10) simulations. The sample size  $N$  is 30 for both the “control” and “perturbed” populations.

610 For the ERA5 reanalysis (Fig. 1), the test we performed is meant to compare the selected El Niño years and the “regular” years. Therefore, the “control” population is the sample of all the years (from May to following April) whose ENSO index exceed neither the El Niño nor the La Niña threshold (sample size  $N = 29$ ) and the “perturbed” population is the sample of El Niño years (sample size  $N = 6$ ).

#### **Appendix D: Pliocene SST proxies**

615 We used Alkenone SST proxy (Uk’37) from ODP sites 1125 (?), 850, 806 (?), 1208, 1021 (?), 607, 856, 847, 982 and 1241 (?). For each site, we averaged the available SST estimates between 4.5 Ma and 3.5 Ma as “Pliocene” SST. In the case of ? (sites 607, 856, 847, 982 and 1241), we took the SST already averaged in Table S1 of their contribution (local SST without correction). For the “control” SST values, we used the modern SST from ?, Table S1 of their contribution. There are two exceptions: for sites 1021 and 806, we considered the near-modern interglacial SST of the time-series as modern SST, because they significantly differ from the actual modern SST (? , Table S1).

620 *Author contributions.* P.M. and J.C.H.C. conceived the experiments and ran the climate simulations, P.M. ran the GEOCLIM simulations, wrote the original manuscript draft, and drafted the figures. J.C.H.C. and N.L.S.-H. contributed to manuscript writing. J.C.H.C and N.L.S.-H. acquired funding and supervised project research.

*Competing interests.* The authors declare no conflict of interest

*Acknowledgements.* Research was supported by NSF Frontier Research in Earth Science grant EAR-1925990 awarded to N.L.S.-H. and J.C.H.C. We thank Natalie Burls for useful discussions on climate dynamics and guidance on the design and interpretation of the climate  
625 simulations. We dedicate this work to the memory of our dear colleague and friend Sarah White, whose work on permanent El Niño and its impacts inspired this manuscript.